MECHANICS OF NONLINEAR BIOMEMBRANES:

APPLICATION TO OPHTHALMOLOGY

A Dissertation

by

FREDEGUSTO GUIDO DAVID

Submitted to the Office of Graduate Studies of
Texas A&M University
in partial fulfillment of the requirements for the degree of

DOCTOR OF PHILOSOPHY

December 2005

Major Subject: Biomedical Engineering

MECHANICS OF NONLINEAR BIOMEMBRANES:

APPLICATION TO OPHTHALMOLOGY

A Dissertation

by

FREDEGUSTO GUIDO DAVID

Submitted to the Office of Graduate Studies of
Texas A&M University
in partial fulfillment of the requirements for the degree of

DOCTOR OF PHILOSOPHY

Approved by:

Chair of Committee,	Jay D. Humphrey
Committee Members,	John C. Criscione
	Jay Walton
	Hsin-i Wu
Head of Department,	Gerald L. Cote

December 2005

Major Subject: Biomedical Engineering

ABSTRACT

Mechanics of Nonlinear Biomembranes:

Application to Ophthalmology. (December 2005)

Fredegusto Guido David, B.S., University of the Philippines;

M.S., University of the Philippines;

M.S., Texas A&M University

Chair of Advisory Committee: Dr. Jay D. Humphrey

Changes in the mechanics of the lens capsule of the eye arising from alterations of its native configuration can lead to undesirable clinical results. One example is the surgical introduction of a hole into the lens capsule and subsequent removal of the cloudy lens during cataract surgery. The adverse effect is secondary cataract on the posterior lens capsule, brought about by a sudden proliferation of lens epithelial cells in the region. Understanding the biomechanics of the anterior lens capsule is necessary in order to model its behavior under various physiological conditions and predict its response to alterations and perturbations such as those during cataract surgery. Such knowledge will help in the improvement of techniques during cataract surgery, and in the design of artificial intraocular lens.

In this study we present, for the first time, results that demonstrate that the anterior lens capsule exhibits non-homogeneity and regionally varying anisotropy. We also compute stresses in the lens capsule due to normal loading conditions and procedures such as a capsulorhexis.

ACKNOWLEDGEMENTS

I would like to thank my committee chair, Dr. Jay D. Humphrey, and my committee members, Dr. Walton, Dr. Criscione and Dr. Wu, for their guidance and invaluable support throughout the course of this research.

Thanks also to my friends and colleagues and the faculty and staff of the Biomedical Engineering Department and the Mathematics Department for making my stay at Texas A&M University enjoyable and fruitful. In particular, I wish to thank my collaborators Ryan, Mark and Sherry; to Leah, Samantha and Emily for their assistance; and to Hyun for her contributions. I would also like to extend my appreciation to the Texas Advanced Technology Program, the National Institutes of Health, and Alcon Laboratories, Inc., Fort Worth Texas, for making my research possible. Special mention goes to Drs. M. Karakelle, K. Chan, and Q. Peng at Alcon for their continued support throughout this project.

Finally, I want to express my gratitude to my father and mother, my two brothers and five sisters for their encouragement.

TABLE OF CONTENTS

LIST OF FIGURES

LIST OF TABLES

CHAPTER I

INTRODUCTION: THE LENS CAPSULE

The lens is a transparent, ellipsoidal-shaped, gel-like structure of the eye whose function is to focus light onto the retina at the back of the eye, similar to a lens in a telescope. The human lens changes shape by movement of the ciliary muscles, a process called accommodation, in order for us to adjust our vision to see near and far objects. The lens is composed mostly of protein and water, and is encased in the lens capsule, a thin membrane made up of collagen.

There is little turnover in the proteins that make up our lens. Most of the proteins in the lens were already present at birth. Over time, some of these proteins may clump together, resulting in a cloudiness of the lens. This is known as a cataract. People with cataracts have blurred vision and have difficulty seeing. Double-vision, reduced color perception, and glares from bright lights are some symptoms of developing cataracts.

Although there are other factors that affect the formation of cataracts, in most instances cataracts are just a natural result of aging. Over half of people in the United States age 65 or older have cataract in at least one eye. In the United States, more than 1.5 million cataract surgeries are performed every year. This makes cataract treatment the number one Medicare expense in the United States.

_____

This dissertation follows the style and format of the *Journal of Biomechanics*.

There are currently no drugs that can be taken to avoid or cure cataracts. The most common treatment for cataracts is extracapsular surgery with phacoemulsification. In this procedure, the surgeon creates a small incision on the edge of the cornea. A hole is created on the lens capsule, the membrane that surrounds the lens. A probe is then inserted in the opening. Ultrasound is used to break up the cloudy lens, which is subsequently extracted. An artificial foldable intraocular lens (IOL) is then inserted through the opening and placed inside the empty lens capsule, which provides structural support for the IOL. This method has replaced older techniques which required larger incisions. Because of the smaller incision, stitches are not needed, and fewer complications arise.

Posterior Capsular Opacification has been the most common complication post-cataract surgery. It occurs when remnant lens epithelial cells (LEC) from extracapsular surgery proliferate and migrate towards the posterior lens capsule. This causes the posterior lens capsule to become opaque, a condition known as "secondary cataract." The incidence rate of PCO based on recent data is around 18% (Apple et al., 2001). This number has gone down from as high as 50% PCO occurrence (within two years of surgery) because of improvements in medical techniques and implant design. The primary treatment for PCO is Nd:Yag laser posterior capsulotomy. Low level laser energy is used to punch holes in the opaque posterior lens capsule, allowing light to pass through. There is usually no recurrence of posterior lens capsule opacification after Nd:Yag laser treatment. In some cases, post-operation side effects, including retinal detachment, raised intraocular pressure and cystoid macular edema may occur. Moreover,

laser treatment is expensive, and secondary cataract treatment is the number two expense for Medicare.

Despite the widely recognized importance of the biomechanics of the lens capsule in normal processes such as accommodation and clinical interventions such as cataract surgery, there has been no prior quantification of the regional, multiaxial, anisotropic behavior of the lens capsule. Krag et al. (1996, 1999, 2003) conducted studies on the mechanical properties of the lens capsule, but their work has been largely based on uniaxial tests on thin strips cut out from the lens capsule. Burd et al. (1999, 2002) have done numerical studies on accommodation, but their results are based on linear elasticity. The bulk of lens capsule research focuses mainly on the qualitative aspects of capsulorhexis and case studies on the effects of IOL design and implantation. Thus, there is a pressing need to conduct experimental and numerical studies on the behavior of the lens capsule because of the significance of understanding the mechanics of the lens capsule.

In this dissertation, we study the mechanical properties of porcine lens capsules (with subsequent parallel studies on human lens capsules). In order to study the stress-strain relationship, we first utilize a custom inverse sub-domain finite element method to estimate the values of material parameters that relate to material stiffness and anisotropy using pressure and strain data obtained via a new bi-plane video-based experimental system. We then use the material parameters and prescribed pressure or applied loads via a forward finite element numerical solution (i.e. weak form) to predict stresses, strains and the deformed geometry of the lens capsule before and after continuous circular capsulorhexis (CCC). Numerical results are compared with experimental data as well as a

plane-stress redistribution patch test solved in strong form (i.e., using differential equations). The last chapter is a brief study on the effects of viscoelasticity on biomechanical applications to a similar membrane—an intracranial saccular aneurysm.

The results of this dissertation show, for the first time, that the anterior lens capsule exhibits non-homogenous, regionally dependent anisotropy. Moreover, this non-homogeneity is favorable to the lens capsule's behavior. This built-in anisotropy appears to homogenize the predicted stress fields in normalcy, which may be teleologically favorable.

CHAPTER II

REGIONAL MULTIAXIAL PROPERTIES

OF THE PORCINE ANTERIOR LENS CAPSULE

Overview

The lens capsule of the eye plays fundamental biomechanical roles in both normal physiological processes and clinical interventions. Heretofore there has been little attention to the mechanical properties of this important membrane, and all analyses have been based on 1-D data. We present, for the first time, results that show that the lens capsule has a complex, regionally-dependent, nonlinear, anisotropic behavior. Specifically, analyzing data from a new biplane video-based test system via a custom nonlinear sub-domain inverse finite element method, we show that the lens capsule is nearly isotropic near the pole but progressively stiffer in the circumferential compared to the meridional direction as one approaches the equator. Such detail should be accounted for in the design of surgical procedures and implants.

Introduction

Despite the widely recognized importance of the biomechanics of the lens capsule in normal processes such as accommodation and clinical interventions such as cataract surgery, there has been no prior quantification of the regional, multiaxial, biomechanical behavior of the lens capsule. Recently, therefore, we developed new experimental techniques and a new experimental system specifically for collecting data in situ on the mechanical behavior of the lens capsule (Heistand et al., 2005a). In this paper, we analyze these recent data using a sub-domain inverse finite element method to determine

best-fit material parameters in 2-D Fung and Choi-Vito hyperelastic constitutive relations. Results are presented for 6 porcine anterior lens capsules.

Consistent with prior uniaxial studies, we find a nonlinear, nearly elastic behavior over finite strains. In addition, however, we show that, independent of the model used, the porcine anterior lens capsule exhibits a strong regionally-dependent anisotropy: the capsule is stiffer in the circumferential compared to the meridional direction as one moves from the central pole to the equator. The potential implications of these findings are discussed within the context of normal development and clinical intervention.

Methods

Experimental Approach. Our experimental techniques and custom test device are described in detail in Heistand et al. (2005a). Briefly, fresh porcine eyes were obtained via overnight shipment from Sioux Preme Inc. (Idaho), the cornea and iris were removed, and the globe was secured within a moldable wax fixture. Twenty-three 40-μm diameter fluorescent microspheres were placed on the anterior lens capsule as overlapping sets of five markers each. These sets extend from the pole (i.e., Y-suture) to the equator along both the minor and major axes (Figure 2.1). Using a 25-gauge needle inserted just under the lens capsule and a saline infusing solution, the lens capsule was cyclically distended using pressures from 0 to 45 mmHg and the resulting motions of the markers were determined in 3-D using the biplane video system. Finally, at the end of the mechanical testing, the anterior capsule was cut free from the lens and posterior capsule and laid atop the lens. This allowed the stress-free reference configuration to be determined locally for each set of markers. Knowing marker motions relative to a reference configuration plus

the applied loads allowed determination of best-fit values of the material parameters for two candidate constitutive relations.
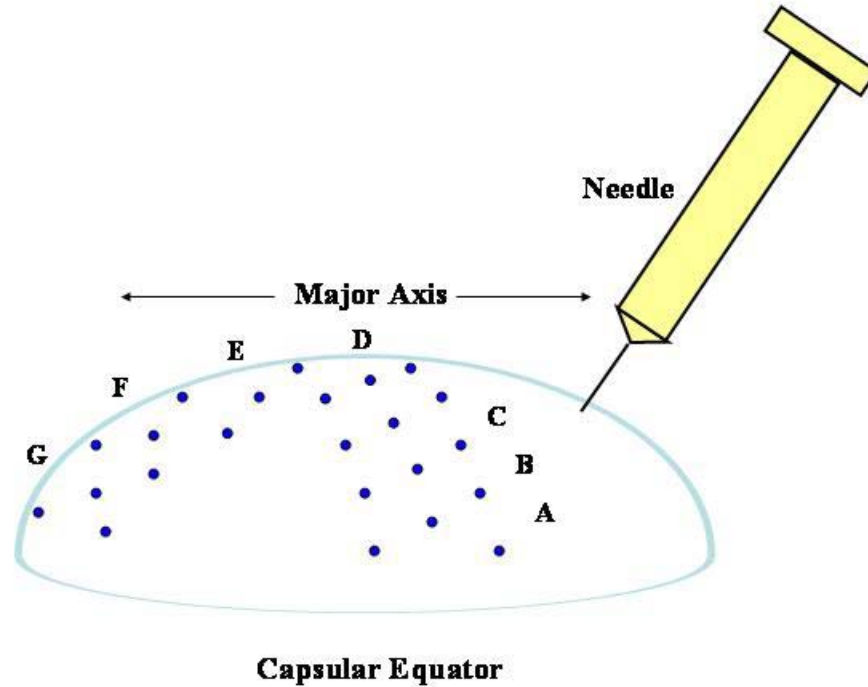
Figure 2.1. Marker arrangement along the anterior lens capsule. Sets A to D lie along the minor axis and sets D to G along the major axis. The center marker of set D is placed on the pole (Y-suture).

Constitutive Framework. The thickness of the porcine anterior lens capsule is approximately 60 μm whereas the radius of curvature is about 8 mm. Hence, given its apparent low bending stiffness (Burd et al., 2002; Heistand et al., 2005a), it is reasonable to treat the capsule mechanically as a membrane. A general pseudoelastic framework for biomembranes can be written as (Humphrey, 2002)

$$\mathbf{T} = \frac{1}{J_{2D}} \mathbf{F}_{2D} \cdot \frac{\partial w}{\partial \mathbf{E}_{2D}} \cdot \mathbf{F}_{2D}^{T} \leftrightarrow T_{\Sigma\Xi} = \frac{1}{J_{2D}} F_{\Sigma\Gamma} F_{\Xi\Delta} \frac{\partial w}{\partial E_{\Gamma\Delta}} \qquad \Sigma,\Xi,\Gamma,\Delta = 1,2 \quad (2.1)$$

where $\mathbf{T}$ is the Cauchy membrane stress (i.e., stress resultant) tensor, $\mathbf{F}_{2D}$ is the 2-D deformation gradient tensor, $J_{2D} = \det \mathbf{F}$, and $\mathbf{E}_{2D} = \left(\mathbf{F}_{2D}^T \cdot \mathbf{F}_{2D} - \mathbf{I} \right)/2$ is the 2-D Green strain tensor. Finally, w is the stored energy function per unit reference area. Because the functional from of w cannot be determined directly from experimental data given our experimental setup, we evaluated two commonly used exponential relations, written in terms of principal strains:

$$w = c\left(e^{Q} - 1\right) \qquad Q = c_1 E_{11}^2 + c_2 E_{22}^2 + 2c_3 E_{11} E_{22} \tag{2.2}$$

the so-called Fung model (with c, c_1, c_2, c_3 material parameters), and

$$w = c\left(e^{Q_1} + e^{Q_2} + e^{Q_3} - 3\right) \qquad Q_1 = c_1 E_{11}^2, \; Q_2 = c_2 E_{22}^2, \; Q_3 = 2c_3 E_{11} E_{22} \tag{2.3}$$

the so-called Choi-Vito model (with c, c_1, c_2, c_3 material parameters). Note that the *1-* and *2-* directions are circumferential and meridional, respectively, for both constitutive models. See Fung (1990), Choi and Vito (1990), Sacks (2003) and Humphrey (2002) for more on these models and their ability to fit soft tissue data.

Inverse Finite Element Method. Given the complex geometry and loading condition, the biomechanics of the lens capsule cannot be studied in closed form. Consequently, we employ a sub-domain inverse finite element approach to determine best-fit material parameters associated with the Fung and Choi-Vito models. Toward this end, we combine a standard Marquardt-Levenberg nonlinear regression with a virtual work based membrane finite element formulation. The latter is based on the principle of virtual work for an inflated membrane:

$$\int_{\Omega_o} \delta w \, dA - \int_{\Omega} p \vec{n} \cdot \delta \vec{x} \, da = 0 \tag{2.4}$$

where p is the measured distension pressure, $\vec{n}$ is a local outward unit normal vector, and $\delta\tilde{x}$ are virtual nodal displacements. Details on the inverse finite element formulation are in Seshaiyer and Humphrey (2003). Briefly, the general computational strategy is to solve the finite element problem individually for each set of 5 markers (i.e., regions A to G, Figure 2.1). The experimentally measured pressure is applied and the measured displacements are prescribed for the 4 corner markers of each set of 5 as displacement boundary conditions. The finite element solution for the (x, y, z) position of the central node is then compared to the measured location at each equilibrium state, with the Marquardt-Levenberg regression finding those values of c, c_1, c_2, c_3 that provide the best fit to data. That is, the finite element solution for the position $\vec{x}_{FEM} = (x, y, z)$ of the central node at each pressured state $k = 1, 2, ..., m$ is used to construct the objective function

$$\varepsilon = \sum_{k=1}^{m} \left\{ \left(\vec{x}_{FEM} - \vec{x}_{EXP} \right) \cdot \left(\vec{x}_{FEM} - \vec{x}_{EXP} \right) \right\}_k \qquad (2.5)$$

which is then minimized, namely, $\partial\varepsilon/\partial c = 0$ and $\partial\varepsilon/\partial c_i = 0$. An implicit assumption is that the properties are homogeneous over each sub-domain (~1 mm x 1 mm compared to dimensions of approximately 9 mm and 8 mm for the major and minor axes diameters of the lens capsule). Consistent with this, we assume a homogeneous deformation within each subdomain and hence use nodal shape functions based on a standard triangular element and a Gaussian quadrature (Szabo and Babuska, 1991).

Following Gruttman and Taylor (1992), it proves convenient to write the strain-energy w in terms of coordinate invariant measures of the deformation rather than principal Green strain (note: Heistand et al. (2005a) show that the circumferential and

meridional directions are principal). Toward this end, it can be shown that equation (2.2) can be rewritten as

$$w = c\left(e^Q - 1\right) \qquad Q = \alpha J_1^2 + 2\beta J_2 + 2\gamma J_1 J_4 + \delta J_4^2 \qquad (2.6)$$

where

$$J_1 = \text{tr } \mathbf{E} = E_{11} + E_{22}$$

$$J_2 = \det \mathbf{E} = E_{11}E_{22} - E_{12}E_{21} \qquad (2.7)$$

$$J_4 = \vec{M}^T \cdot \mathbf{E} \cdot \vec{M}$$

with $\vec{M}$ a unit vector denoting the preferred directions of the material relative to the reference configuration. Without loss of generality, and consistent with Heistand et al. (2005a), we let $\vec{M} = \begin{bmatrix} 1 & 0 \end{bmatrix}^T$, or $J_4 = E_{11}$. Finally, note that Humphrey (2002) showed that $c > 0$ and $c_i > 0$ (i = 1, 2, 3) for equation (2.2) to yield physically reasonable results whereas Holzapfel (2000) showed further that $c_1 c_2 > c_3^2$ to ensure convexity. A weaker condition $c_1 > c_3$ and $c_2 > c_3$ guarantees the material behaves well under uniaxial loading (Appendix) and is a sufficient condition for convexity. In terms of equation (2.2), with $c_1 = \alpha + 2\gamma + \delta$, $c_2 = \alpha$, $c_3 = \alpha + \gamma$ and thereby $\alpha = c_2 > 0$, $\beta = 0$, $\gamma = c_3 - c_2$, $\delta = c_1 + c_2 - 2c_3$, then

$$\alpha > 0, \ \beta = 0, \ \gamma < 0 \text{ and } \delta > 0. \qquad (2.8)$$

Of course, if isotropic, $Q = \alpha J_1^2 + 2\beta J_2$ with $\alpha = c_1 = c_2$, $\gamma = \delta = 0$ and $\beta = c_3 - c_2$.

Similarly, for Equation (2.3), an invariant form of the Choi-Vito model can be written as

$$Q_1 = c_1 J_4^2, \ Q_2 = c_2 \left(J_1 - J_4\right)^2, \ Q_3 = 2c_3 J_4 \left(J_1 - J_4\right) \qquad (2.9)$$

where the invariants are given as in (2.7). Note that if $\vec{M} = \begin{bmatrix} 1 & 0 \end{bmatrix}^T$, as above, then equation (2.9) reduces directly to (2.3). Realize that the proposed invariant form (2.9) works in the specific case where the preferred direction is either the 1 or 2 direction and when $\mathbf{E}$ is diagonal. If the material is isotropic, for instance, then a different strain-energy model is needed.

It appears that a sufficient condition for convexity of (2.3) is that $c_1, c_2, c_3 > 0$ whenever $c > 0$. Further, a weak restriction can be imposed on the material parameters by $c_1 > c_3$ and $c_2 > c_3$ (see Appendix).

Patch tests. Finite element solutions should be checked via comparison with exact solutions. The simplest problem for the pressurization of a nonlinear membrane is the uniform inflation of a sphere. If the membrane is a perfect sphere deforming into another sphere, which requires in-plane isotropy, then we have $\mathbf{E} = \frac{1}{2} diag[\lambda^2 - 1, \lambda^2 - 1]$, where λ is the stretch ratio. For example, for the isotropic Fung strain-energy function, equation (2.2) reveals that we need:

$$\frac{\partial w}{\partial E_{\Gamma\Delta}} = ce^Q \frac{\partial Q}{\partial E_{\Gamma\Delta}}, \qquad \frac{\partial Q}{\partial E_{\Gamma\Delta}} = \frac{\partial Q}{\partial J_1} \frac{\partial J_1}{\partial E_{\Gamma\Delta}} + \frac{\partial Q}{\partial J_2} \frac{\partial J_2}{\partial E_{\Gamma\Delta}}. \tag{2.10}$$

Note, therefore, that for the isotropic Fung model,

$$\frac{\partial Q}{\partial J_1} = 2\alpha J_1, \quad \frac{\partial Q}{\partial J_2} = 2\beta \tag{2.11}$$

and

$$\frac{\partial J_1}{\partial E_{11}} = 1, \qquad \frac{\partial J_1}{\partial E_{22}} = 1, \qquad \frac{\partial J_2}{\partial E_{11}} = E_{22}, \qquad \frac{\partial J_2}{\partial E_{22}} = E_{11}. \tag{2.12}$$

Hence,

$$\frac{\partial w}{\partial E_{11}} = ce^{Q}\left(2\alpha E_{11} + 2(\alpha + \beta)E_{22}\right) = ce^{Q}(2\alpha + \beta)\left(\lambda^2 - 1\right) \tag{2.13}$$

and similarly for other terms. Thus from equation (2.2),

$$T_{11} = T_{22} = T = ce^{Q}(2\alpha + \beta)\left(\lambda^2 - 1\right). \tag{2.14}$$

From equilibrium, the uniform Cauchy wall tension is determined from the applied pressure and geometry via

$$T = \frac{Pa}{2} \Leftrightarrow P = \frac{2T}{a} \tag{2.15}$$

where a is the deformed radius ($a = \lambda A$ where A is the undeformed radius). Thus, the experimental pressure is P_{EXP} and the theoretically calculated P_{THEORY} is

$$P_{THEORY} = \frac{2c(2\alpha + \beta)\left(\lambda^2 - 1\right)\exp\left\{\frac{1}{2}(2\alpha + \beta)\left(\lambda^2 - 1\right)^2\right\}}{a}. \tag{2.16}$$

We see that for the inflation of a sphere, equivalent to an in-plane equibiaxial test, the system reduces to one equation with two independent parameters, namely c and $2\alpha + \beta = const$. A plot of the error structure for the spherical (equibiaxial) patch test turns out to be a parabolic cylinder (Figure 2.2), demonstrating that the family of solutions that yield a minimum error lie along a straight line on the vertex of the parabolic cylinder. This shows that the spherical test is not useful when trying to solve for the values of the material parameters via an inverse solver (although the sphere is a useful patch test for the forward and semi-inverse solvers, once the parameters are known).

Conversely, a non-equibiaxial test is useful for it generates two independent equations $T_1 = T_1(\lambda_1, \lambda_2)$ and $T_2 = T_2(\lambda_1, \lambda_2)$ in terms of two stretches λ_1, λ_2. For a general anisotropic Fung model,

$$\frac{\partial Q}{\partial J_1} = 2c_2 J_1 + 2(c_3 - c_2)J_4, \quad \frac{\partial Q}{\partial J_4} = 2(c_3 - c_2)J_1 + 2(c_1 + c_2 - 2c_3)J_4, \quad (2.17)$$

thereby allowing the principal stress resultants to be computed easily via (2.1).

These findings on the equibiaxial patch test reveal a reason for a sub-optimal validation in Seshaiyer and Humphrey (2003) and will prove important in the interpretation of results below. Note, however, that the non-equibiaxial "patch test" performed by Seshaiyer and Humphrey revealed that the sub-domain inverse finite element used herein is robust.
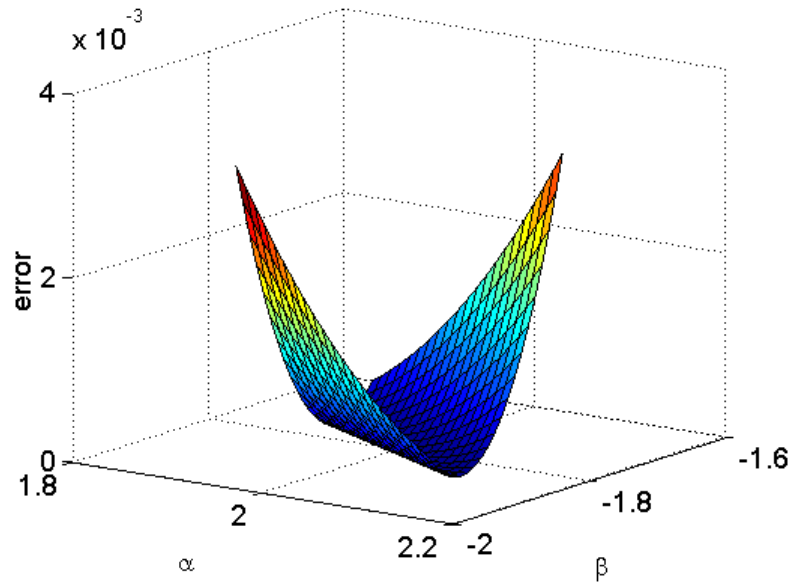
Figure 2.2. Error structure of equibiaxial stretch simulation. The error (vertical axis) is plotted against the material parameters α and β (horizontal plane). The error structure takes the form of a parabolic cylinder. Note that there is no unique solution (indeed, the family of solutions lie along a line), hence the result obtained by the inverse method depends on the initial guess.

Equibiaxial and Uniaxial Responses. Whereas the sub-domain method provides complete information on the properties (given the assumed forms of w), the results are more easily visualized via standard stress-stretch type plots. In particular, equibiaxial

stretching does reveal well the multiaxial behavior including anisotropy. Given $\mathbf{F}_{2D} = diag[\lambda, \lambda]$, the resulting $\mathbf{T}$-λ plots can be reconstructed with

$$T_{11} = \frac{1}{\lambda^2}\left(\lambda^2\right)\frac{\partial w}{\partial E_{11}}\bigg|_{E_{11}=E_{22}=\lambda} \quad ; \quad T_{22} = \frac{1}{\lambda^2}\left(\lambda^2\right)\frac{\partial w}{\partial E_{22}}\bigg|_{E_{11}=E_{22}=\lambda} \tag{2.18}$$

which is straightforward. It is interesting to note that for the equibiaxial stretching test, the Fung model requires that

$$\frac{T_{11}}{T_{22}} = \frac{c_1 + c_3}{c_2 + c_3} \tag{2.19}$$

which reveals a constant ratio for all λ. In contrast, the Choi-Vito model requires that

$$\frac{T_{11}}{T_{22}} = \frac{c_1 \exp\left(\frac{c_1}{4}\left(\lambda^2-1\right)^2\right) + c_3 \exp\left(\frac{c_3}{2}\left(\lambda^2-1\right)^2\right)}{c_2 \exp\left(\frac{c_2}{4}\left(\lambda^2-1\right)^2\right) + c_3 \exp\left(\frac{c_3}{2}\left(\lambda^2-1\right)^2\right)} \tag{2.20}$$

which is less restrictive than the Fung model.

Additionally, because nearly all prior results on the lens capsule (e.g. Krag and Andreassen, 2003) present uniaxial stress-stretch results plots, it is useful to consider these as well. Let $\mathbf{F}_{2D} = diag[\lambda, \mu]$ where λ is a stretch ratio in the primary stretching direction and μ is in the orthogonal (thinning) direction. Hence, $T_{11} > 0$ and $T_{22} = 0$ for a thin uniaxially loaded strip. In this case,

$$T_{11} = \frac{1}{\lambda\mu}\lambda^2\frac{\partial w}{\partial E_{11}}\bigg|_{\lambda_1=\lambda,\lambda_2=\mu} \quad , \quad T_{22} = \frac{1}{\lambda\mu}\mu^2\frac{\partial w}{\partial E_{22}}\bigg|_{\lambda_1=\lambda,\lambda_2=\mu} = 0. \tag{2.21}$$

For the Fung model,

$$T_{11} = \frac{\lambda}{\mu}ce^Q\left(c_1(\lambda^2-1)+c_3(\mu^2-1)\right) > 0 \tag{2.22}$$

$$T_{22} = \frac{\mu}{\lambda} c e^{Q} \left(c_2 (\mu^2 - 1) + c_3 (\lambda^2 - 1) \right) = 0 \Rightarrow \mu = \sqrt{1 + \frac{c_3}{c_2} \left(1 - \lambda^2 \right)} \quad \forall \lambda \geq 1. \quad (2.23)$$

Note that for a physically realistic deformation ($\mu > 0$),

$$\frac{c_2}{c_3} > \lambda^2 - 1. \quad (2.24)$$

Similarly, for the uniaxial stretch of the Choi-Vito model,

$$T_{11} = \frac{\lambda}{\mu} \left(c_1 (\lambda^2 - 1) e^{Q_1} + c_3 (\mu^2 - 1) e^{Q_3} \right) \quad (2.25)$$

$$T_{22} = \frac{\mu}{\lambda} \left(c_2 (\mu^2 - 1) e^{Q_2} + c_3 (\lambda^2 - 1) e^{Q_3} \right) = 0.$$

Since the *2*-direction is traction-free,

$$c_2 \left(\mu^2 - 1 \right) e^{\frac{1}{4} c_2 \left(\mu^2 - 1 \right)^2} + c_3 \left(\lambda^2 - 1 \right) e^{\frac{1}{2} c_3 \left(\lambda^2 - 1 \right) \left(\mu^2 - 1 \right)} = 0, \quad (2.26)$$

which provides a restriction on μ given λ, which can be enforced numerically.

Results

Parameter Values. Pressure-strain data for 6 porcine eyes were used to obtain best-fit values for the material parameters. Note that, in all of our experiments, at least one of the markers in set A fell off, hence rendering the data incomplete for set A. There may also be certain marker sets missing in a few porcine eyes, as one can observe from Figure 2.3a-b. Figure 2.3a shows the results for material parameter c (in N/mm) for the Fung model. An ANOVA revealed that this parameter is not significantly different for the multiple marker sets, at greater than 99% confidence. Although the porcine donors were of similar age, there were individual variations in the stiffness of the lens capsule. In Figure 2.3b, we present the associated results for material parameters c_1 and c_2 as a ratio. Recall that c_1 reflects the stiffness of the material in the *1-* or circumferential direction,

whereas c_2 reflects the stiffness in the *2*- or meridional direction. We observe a distinct trend: the ratio c_1/c_2 is much larger near the equator (towards sets A and G) and much smaller towards the pole (set D). At the exact pole, the ratio in theory must be equal to 1 if this is a symmetry axis. The central node of each marker set is approximately 1 mm from the adjacent central node. We hereby propose the following approximate formula for the ratio of the Fung material parameters c_1 and c_2 as a function of the arc length s from the pole (in mm):

$$\frac{c_1}{c_2} = 2^{ks} \tag{2.27}$$

with κ a non-dimensionalizing constant equal to 1 mm^{-1}.

Table 2.1a lists the mean values of the material parameters. We found little variation in material parameter c_3, which was always small compared to the value of c_1 and c_2, thus satisfying both the physical and convexity conditions.

Obtaining best-fit values when there are exponential and linear parameters is a delicate procedure. We addressed this post-hoc by using the mean values of c for each porcine sample, fixing c constant, then re-running the sub-domain inverse finite element program to calculate best-fit values for c_1, c_2 and c_3 (Table 2.1b). The calculated values changed, but the ratios c_1/c_2 were approximately maintained, thus preserving the regional anisotropy as seen in Table 2.1a.

Figure 2.3. Fung material parameters based on porcine lens capsule data. Graphs show inverse sub-domain finite element results for **(a)** material parameter c (in N/mm), and **(b)** the ratio of material parameters c_1/c_2 (ratio of circumferential to meridional "stiffness") for 6 porcine anterior lens capsules. ANOVA tests reveal no significant variation between groups of marker sets ($p < 0.01$) for c. Note that parameters were difficult to estimate at set D, presumably because of the near equibiaxial strain near the pole (cf. Heistand et al., 2005a).

Table 2.1. Average values of Fung material parameters for porcine eyes. The values in **(a)** show the calculated values for each marker set averaged over 6 porcine anterior lens capsules. The values in **(b)** are obtained by fixing the values of c and c_3 prior to regression analysis, then averaged over 6 porcine anterior lens capsules. The RMS error was ~0.05 mm, close to the actual video resolution for marker tracking.

(a)

	c (N/mm)	c_1	c_2	c_3	*Error*
A					
B	0.000745	33.02	4.56	1.15	0.05
C	0.000584	22.16	12.08	1.81	0.06
D	0.000614	13.37	14.15	0.95	0.05
E	0.000581	21.20	14.62	0.86	0.04
F	0.000511	30.27	8.72	0.88	0.03
G	0.000600	46.73	3.67	0.59	0.05

(b)

	c (N/mm)	c_1	c_2	c_3	*Error*
A					
B	0.000592	38.06	4.97	1.00	0.06
C	0.000592	23.30	13.11	1.00	0.04
D	0.000500	13.92	13.15	1.00	0.05
E	0.000592	20.80	14.34	1.00	0.04
F	0.000562	28.97	8.16	1.00	0.03
G	0.000683	43.85	3.75	1.00	0.06

Parameter estimation using the Choi-Vito constitutive assumption was used for comparison. Figure 2.4a shows the estimated values of c (in N/mm), Figure 2.4b shows the ratios c_1/c_2, Table 2.2a shows average values of the material parameters for the 6 porcine eyes, and Table 2.2b shows average values for a fixed value of c. Note that even with a different constitutive model assumption, the graphs show the same trend in both the near uniformity of c and the changing ratio of circumferential to meridional stiffness, an indirect indication of regionally different properties.
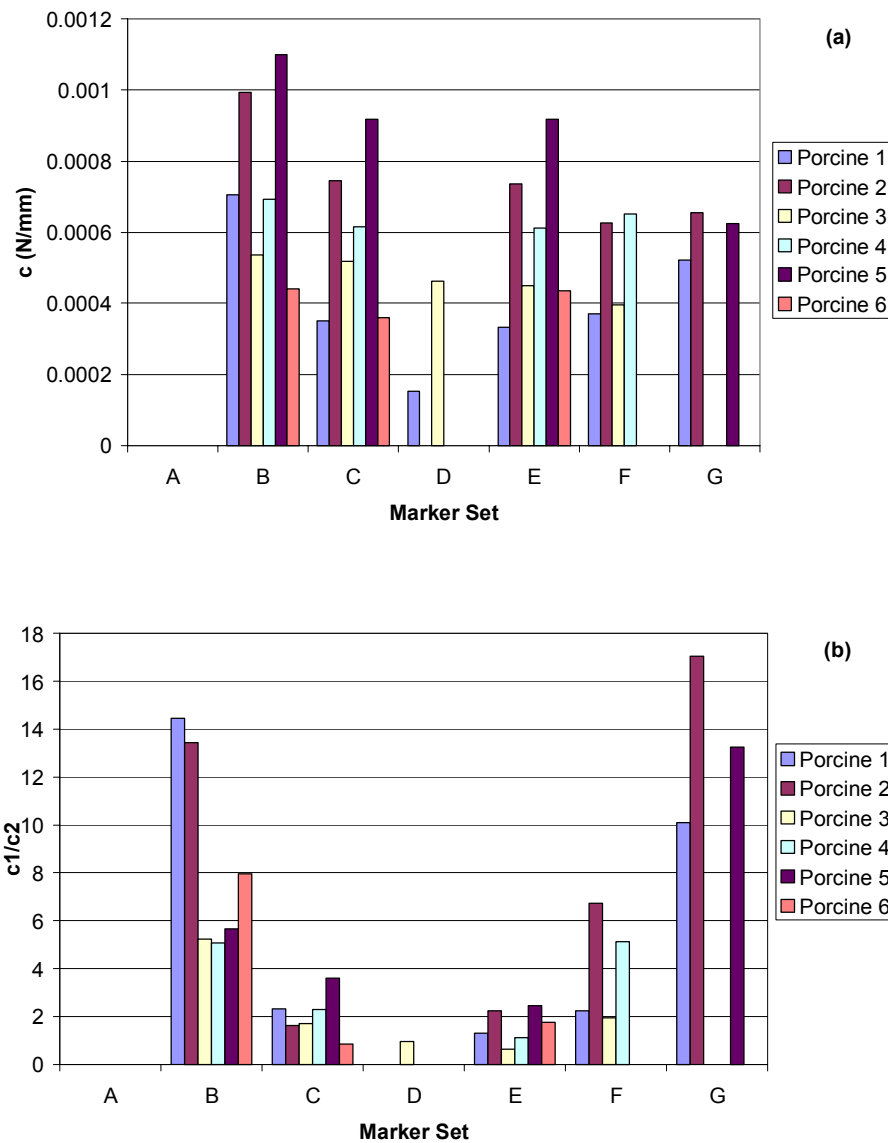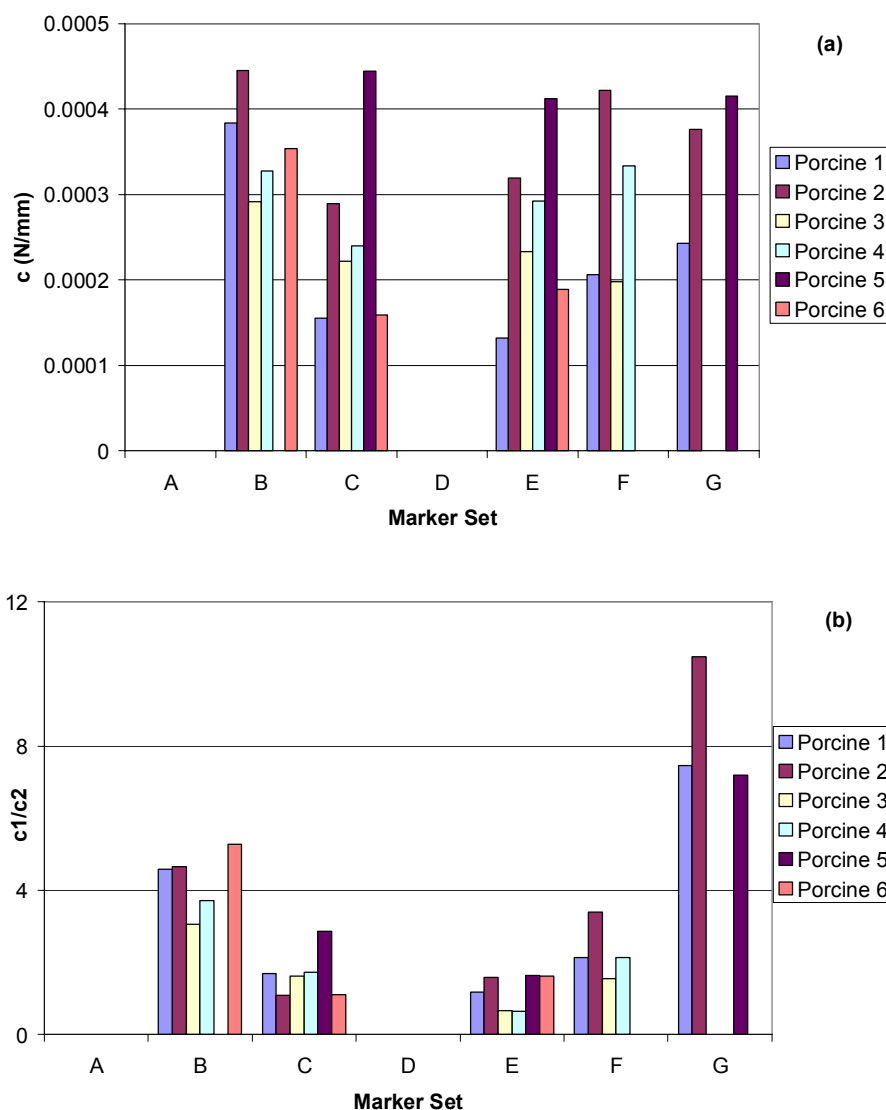
Figure 2.4. Choi-Vito material parameters based on porcine lens capsule data. Charts show inverse sub-domain finite element results for **(a)** material parameter c (in N/mm), and **(b)** the ratio of material parameters c_1/c_2 (ratio of circumferential to meridional "stiffness") for 6 porcine anterior lens capsules. ANOVA tests reveal no significant variation between groups of marker sets ($p < 0.01$) for c, as in the Fung case.

Predicted Stress-Strain Behaviors. After estimating the material parameters, one can calculate the predicted circumferential and meridional stresses for any strain field in post-processing. We considered three simulations: uniaxial loading in either the circumferential or the meridional direction and an equibiaxial stretch. The four stress-strain plots (showing the two stresses in the equibiaxial test) using averages of the

material parameters obtained from set F (Table 2.1b) are shown in Figure 2.5. The choice of set F is to facilitate comparison with experimental results of Krag and Andreassen (1996), who conducted uniaxial strain tests on 100μm-wide rings excised from around that area of the lens capsule. Note that our results show higher stresses at the same strains compared with Krag's data. However, if we fix c constant, say, c = 0.01 N/mm, and obtain best-fit values for c_1, c_2 and c_3 (e.g. c_1 = 3.27, c_2 = 1.32, c_3 = 0.1) we obtain stress-strain curves that resemble Krag and Andreassen's results more closely (Figure 2.6).

Table 2.2. Average values of Choi-Vito parameters for porcine eyes. The values in **(a)** show the calculated values for each marker set, averaged over 6 porcine anterior lens capsules. The values in **(b)** are obtained by fixing the values of c and c_3 prior to regression analysis, then averaged over 6 porcine anterior lens capsules.

(a)

	c (N/mm)	C_1	c_2	c_3	error
A					
B	0.000360	51.55	12.54	3.79	0.04
C	0.000252	45.60	29.64	7.25	0.03
D	0.000213	4.94	29.06	3.81	0.05
E	0.000263	40.20	35.30	3.44	0.03
F	0.000290	48.62	22.14	0.65	0.03
G	0.000415	52.66	7.32	0.84	0.05

(b)

	c (N/mm)	C_1	c_2	c_3	error
A					
B	0.000292	60.62	16.26	1.00	0.05
C	0.000292	44.89	29.94	1.00	0.03
D	0.000250	5.43	27.58	1.00	0.05
E	0.000292	39.33	33.35	1.00	0.03
F	0.000288	48.81	22.18	1.00	0.03
G	0.000400	53.30	7.44	1.00	0.04

Similarly, the uniaxial and equibiaxial responses are shown in Figure 2.7 for the Choi-Vito model, using the values for set F shown in Table 2.2b.
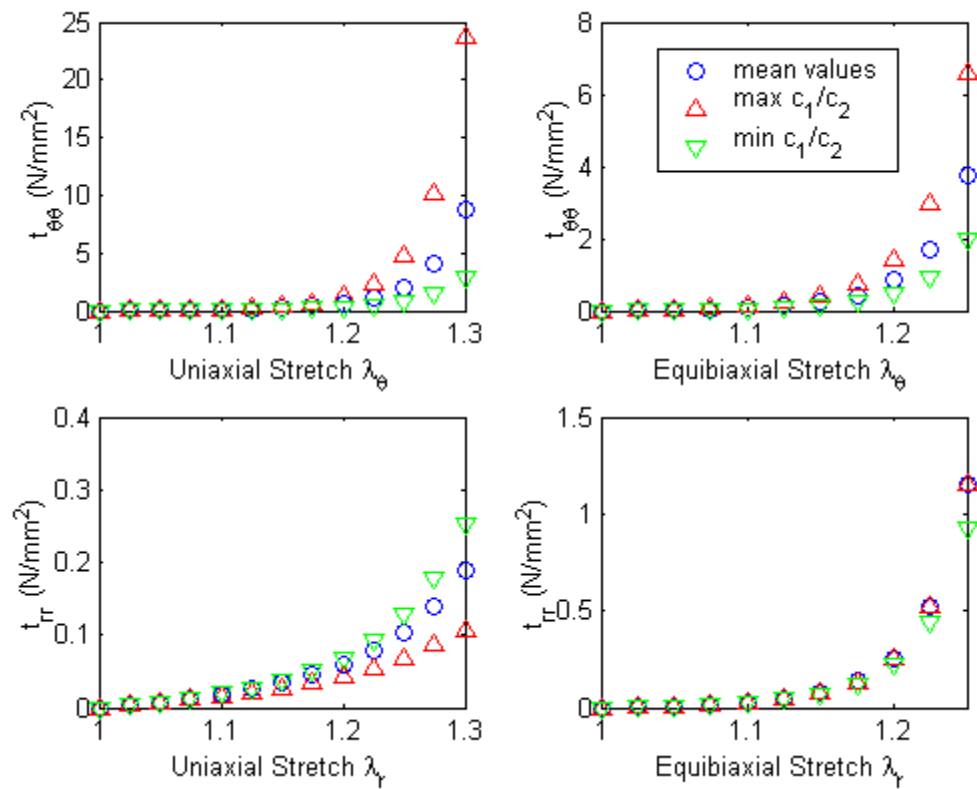
Figure 2.5. Fung model stress-strain simulations. Simulations are based on material parameters for set F from Table 2.1b. Left panels show stresses due to uniaxial stretch tests in circumferential and meridional directions, right panels show stresses due to equibiaxial stretch test.

Figure 2.6. Pseudo-Krag uniaxial stretch simulation. Based on Fung model, showing uniaxial stretch test in circumferential direction using fixed material parameter c = 0.01, other parameters calculated, for set F.

Figure 2.7. Choi-Vito model stress-strain simulations. Simulations are based on material parameters for set F from Table 2.2b. Left panels show stresses due to uniaxial stretch tests in circumferential and meridional directions, right panels show stresses due to equibiaxial stretch test.
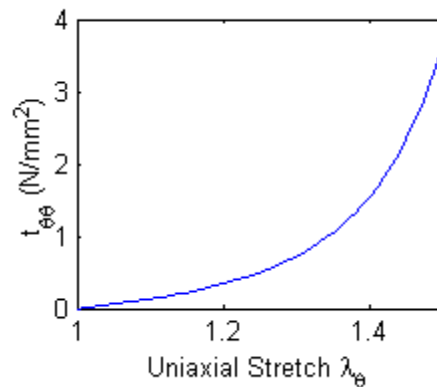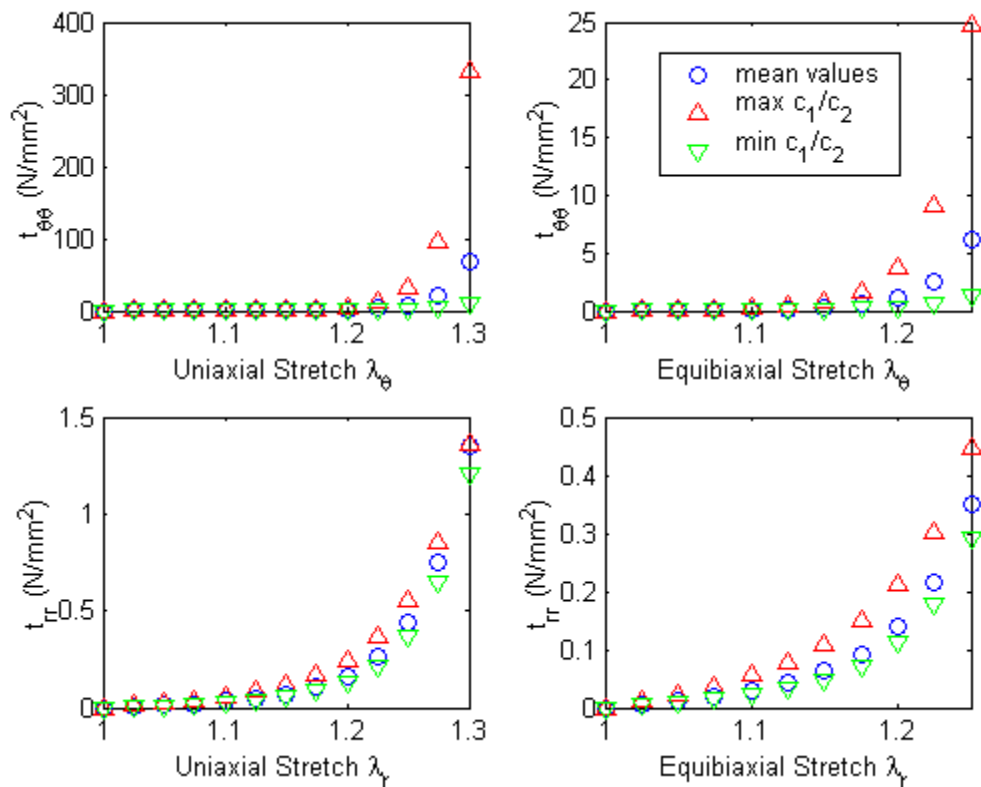
Discussion

Remarkably, this is the first quantification of the multiaxial properties of the lens capsule within the context of nonlinear elasticity. Rather, most prior studies simply report a single value for a Young's modulus $E = 2$ to 6 MPa and Poisson's ratio $\nu = 0.47$; see, for example, Krag et al. (1994) or Burd et al. (2002). Hooke's law is inappropriate for a material that exhibits a nonlinear material behavior over finite strains and, as we show herein, isotropy is likewise inappropriate, except possibly at the pole. One notable exception is the work by Krag and Andreassen (1996) who report a highly nonlinear

stress-strain behavior and an elastic modulus of ~0.5 MPa at 40% strain; they do not propose a stress-strain relation, however.

There are, of course, multiple measures of stiffness in finite elasticity. One of the simplest, and most straightforward, is

$$K_{\Sigma\Xi\Gamma\Delta} = \frac{\partial^2 w}{\partial E_{\Sigma\Xi}\partial E_{\Gamma\Delta}}.$$

(2.28)

For the Fung model, therefore,

$$K_{1111} = 2ce^Q\left(c_1 + 2(c_1 E_{11} + c_3 E_{22})^2\right),$$

(2.29)

$$K_{2222} = 2ce^Q\left(c_2 + 2(c_2 E_{22} + c_3 E_{11})^2\right),$$

whereas for the Choi-Vito model,

$$K_{1111} = 2c\left(c_1 e^{Q_1} + 2c_1^2 E_{11}^2 e^{Q_1} + 2c_3^2 E_{22}^2 e^{Q_3}\right),$$

(2.30)

$$K_{2222} = 2c\left(c_2 e^{Q_2} + 2c_2^2 E_{22}^2 e^{Q_2} + 2c_3^2 E_{11}^2 e^{Q_3}\right).$$

Given that it appears that the in vivo prestretch is, on average, about 10% equibiaxially, (Heistand et al., 2005), note that based on our findings mean values of "stiffness" at set F are

$$\left.\begin{array}{l} K_{1111}(\lambda_1 = \lambda_2 = 1.1) = 0.05 \text{ N/mm} \\ K_{2222}(\lambda_1 = \lambda_2 = 1.1) = 0.015 \text{ N/mm} \end{array}\right\} \text{ Fung}$$

(2.31)

or

$$\left.\begin{array}{l} K_{1111}(\lambda_1 = \lambda_2 = 1.1) = 0.50 \text{ N/mm} \\ K_{2222}(\lambda_1 = \lambda_2 = 1.1) = 0.05 \text{ N/mm} \end{array}\right\} \text{ Choi - Vito}.$$

(2.32)

Hence, if we assume a mean value of the undeformed thickness to be $H = 60$ μm, then the stiffness would range from 0.25 to 0.83 MPa for the Fung model and 0.83 to 8.3 MPa for

the Choi-Vito model at 10% strain (compared to about 20-25 MPa obtained by Krag et al.).

Of most importance, and interest, however, is that the present findings suggest that the lens capsule exhibits regionally-varying material symmetry – from near isotropy at the pole (Y-suture) to progressively stiffer in the circumferential (compared to meridional) direction as one approaches the equator. Although there are no comparable data in the literature to which to contrast these results, it is noteworthy that regional variations have been reported in diverse tissues, as, for example, the heart wall (Novak et al., 1994) and cartilage (Shah et al., 1998). More closely related to this issue, however, Ryan and Humphrey (1999) presented finite element simulations for model intracranial saccular aneurysms that suggested that regional variations in material symmetry in distended biomembranes, fixed around their periphery, can homogenize the stress field, which appears favorable teleologically based on our growing understanding of mechanobiology. In particular, Ryan and Humphrey showed that for wide-necked lesions (geometry similar to the lens capsule), a nearly homogenous stress field can be achieved if the tissue becomes progressively stiffer in the circumferential direction (relative to meridional) and if the strongest anisotropy is localized closest to the neck. Remarkably, without prior bias towards these earlier computational predictions, the present experimental findings are in close agreement, thereby suggesting that the lens epithelial cells that produce and maintain the lens capsule may act cooperatively to ensure that local activity affects the mechanical environment globally (more likely most dramatically during development). This is a particularly provocative hypothesis given the potential redistribution of stress or strain (cf. David and Humphrey, 2004; Heistand et al., 2005b)

in the lens capsule due to clinical interventions such as cataract surgery and the altered cellular activity thereafter. Clearly, we must understand better the native stress/strain environment, the mechanobiological response, and the potential changes therein due to clinical interventions.

Although this work has attempted to advance our understanding of lens capsule properties by addressing the multiaxial and potentially regionally-dependant characteristics for the first time, there remains a need for continued improvement. Our experimental approach preserves native geometry and boundary conditions, but it does not allow the functional form of w to be determined directly from data. This, coupled with a lack of detail on the microstructure, forced us to quantify properties in terms of candidate forms for w. The Fung and Choi-Vito models both describe the behavior of various soft tissues well under many conditions, but both are limited. There is a need for improved constitutive descriptors. The near equibiaxial strains near the pole (cf. Figure 10 in Heistand et al., 2005a) also renders the inverse finite element method ill-conditioned there (recall our findings for the equibiaxial patch test in Figure 2.2), which must also be addressed. It is fortuitous, however, that the apparent trend (cf. Equation 2.27) is nonetheless consistent across both models, even at the pole. Finally, the boundary conditions at the equator (i.e., ciliary processes) must be understood better. Although our sub-domain method avoided this lack of information at the equator, this critical aspect of capsular biomechanics must be quantified if we wish to understand the process of accommodation.

In conclusion, the anterior lens capsule exhibits a complex, nonlinear, regionally-dependent anisotropic behavior which may reflect an underlying mechanobiologic

optimization during development. Perturbations from this native mechanical environment due to clinical intervention should thus be studied within this context, with the goal of minimizing errant healing responses via improved clinical procedures or devices.

CHAPTER III

FINITE ELEMENT MODEL OF STRESSES IN THE ANTERIOR

LENS CAPSULE: IMPACT OF A CAPSULORHEXIS

Overview

Continuum biomechanics continues to aid in the design of clinical procedures as well as biomedical devices. Such design necessitates details on the biomechanical properties and the use of appropriate methods of analysis, however. In this paper, we use a fully nonlinear, virtual work based finite element method to study the stress field in the anterior lens capsule of the eye before and after the clinical procedure called continuous circular capsulorhexis (CCC). The analysis shows that recently measured regional variations in material symmetry yield a nearly uniform and equibiaxial stress field in normalcy. Moreover, a CCC markedly perturbs the stress field from normalcy, increasing the circumferential stress and decreasing the meridional stress, thereby yielding a highly non-uniform, non-equibiaxial field. These findings are discussed in terms of potential implications to the mechanobiology.

Introduction

The lens capsule of the eye is a thin biomembrane that invests the lens and thereby plays key roles in normal physiological functions as well as multiple clinical procedures. For example, we previously hypothesized that the partial opacification of the posterior lens capsule that can occur secondary to cataract surgery is due in large part to perturbations in the stress/strain fields in the anterior lens capsule and associated mechanobiological responses by the lens epithelial cells. Although the lens capsule has a

relatively simple geometry and microstructure, studying the associated biomechanics demands appropriate numerical methods. In this paper, we present a fully nonlinear finite element analysis of the normal stress and strain fields in the anterior lens capsule and explore changes therein due to a common surgical procedure called a continuous circular capsulorhexis (CCC). Moreover, we study the potential roles of recently measured regional variations in material symmetry and likewise the effects of different boundary conditions at the equator.

We show that regional variations in anisotropy tend to homogenize the nearly equibiaxial stress field, which appears favorable teleologically, but that a CCC creates a highly non-homogenous and non-equibiaxial state of stress, which may initiate a strong mechanobiological response by the resident lens capsule epithelial cells.

Methods

Geometry. The lens capsule is an ellipsoidally-shaped, transparent membrane that consists primarily of type IV collagen and sulphated glycosaminoglycans, which give it nearly elastic properties. The anterior lens capsule connects to the posterior lens capsule along an imaginary plane, with the anterior capsule being flatter compared to the posterior capsule. At this so-called equator, the dimension of the porcine lens capsule is about 9 mm along the major axis and about 8 mm along the minor axis; the ratio of the major axis to the height at the pole is about 6:1. The mean thickness of the porcine anterior lens capsule is about 60μm and it is thinnest at the pole. The ratio of the thickness of the anterior lens capsule to its radial dimension is thus very small (~0.01). Moreover, the lens capsule exhibits negligible bending stiffness, thus it is reasonable to assume the anterior lens capsule behaves mechanically as a membrane. Heistand et al.

(2005a) showed further that the lens capsule is nearly hyperelastic as it exhibits negligible creep or hysteresis under slow cyclic stretching.

Because the major and minor axes along the equator of the lens capsule differ by only about 10%, we assume axisymmetry for simplicity. For example, a simple surface geometry that estimates the diameter and height of the anterior lens capsule, with a zero derivative at the pole, is a smooth paraboloid given by

$$x_3 = \frac{3}{2} - \frac{2}{27}(x_1^2 + x_2^2)^2,$$

(3.1)

with x_3 denoting the height direction and x_1 and x_2 the in-plane dimensions, all in mm.

Kinematics and Linear Momentum Balance. The formulation employed below follows Gruttman and Taylor (1992) and Kyriacou et al. (1996). Let $\vec{X}$ be the 3-D reference position of a material particle on the surface of the anterior lens capsule, and let $\vec{x}$ be its corresponding 3-D deformed position. Using 2-D convecting coordinates, we have $\vec{X} = \vec{X}(\xi^1, \xi^2)$ and $\vec{x} = \vec{x}(\xi^1, \xi^2)$. For numerical convenience, however, we define local orthogonal coordinates $\{s_i\}$, thus $\vec{X} = \vec{X}(s_1, s_2)$ and $\vec{x} = \vec{x}(s_1, s_2)$ with orthonormal basis $\vec{t}_j = \dfrac{\partial \vec{X}}{\partial s_j}$. The right Cauchy-Green tensor can now be calculated by

$$\mathbf{C} = \frac{\partial \vec{x}}{\partial s_\Sigma} \cdot \frac{\partial \vec{x}}{\partial s_\Xi} t_\Sigma \otimes t_\Xi \qquad \Sigma, \Xi = 1, 2 \,.$$

(3.2)

A finite element analysis of an inflated membrane can be accomplished using the virtual work principle:

$$\int_{\Omega_0} \delta w \, dA = \int_{\Omega} p \vec{n} \cdot \delta \vec{x} \, da - \int_{\partial \Omega} \vec{T}^n \cdot \delta \vec{x} \, da$$

(3.3)

where w is a strain energy function per undeformed area, p is the distending pressure (converted from mmHg to MPa), $\vec{n}$ is an outward unit normal vector, $\delta\vec{x}$ is a virtual displacement, and $\vec{T}^n$ is the traction applied on some boundary $\partial\Omega$ of the deformed surface Ω (Ω_0 is the undeformed surface).

Constitutive Equation. In order to solve the stress-strain problem, a form of the strain energy function must be specified. In this study, we consider a common form used for soft tissue, specifically the 2-D Fung exponential given by

$$w = c\left(e^Q - 1\right), \qquad Q = c_1 E_{11}^2 + c_2 E_{22}^2 + 2c_3 E_{11} E_{22} \qquad (3.4)$$

where the c and c_i's are material parameters, the *1* and *2* subscripts denote circumferential and meridional directions, which are principal directions in the lens capsule, and the Green strain is $\mathbf{E} = \frac{1}{2}(\mathbf{C} - \mathbf{I})$ where $\mathbf{I}$ is the identity tensor. In practice, it is more convenient numerically to express the strain energy function in terms of the invariants of $\mathbf{E}$ rather than the principal strains (which can be obtained trivially from the invariants of $\mathbf{C}$). Thus we have w in (3.4), with

$$Q = \alpha J_1^2 + 2\beta J_2 + 2\gamma J_1 J_4 + \delta J_4^2 \qquad (3.5)$$

where the invariants are: $J_1 = \mathrm{tr}\mathbf{E} = E_{11} + E_{22}$, $J_2 = \det\mathbf{E} = E_{11}E_{22} - E_{12}E_{21}$, and $J_4 = \vec{M}^T \cdot \mathbf{E} \cdot \vec{M}$, with $\vec{M}$ a unit vector denoting the preferred (fiber) direction. Based on experimental findings of Heistand et al. (2005a), we assume that the lens capsule typically has a circumferential preferred direction. Hence, $\vec{M} = \begin{bmatrix} 1 & 0 \end{bmatrix}^T$ and

$$\alpha = c_2, \beta = 0, \gamma = 2(c_3 - c_2) \text{ and } \delta = c_1 + c_2 - 2c_3. \qquad (3.6)$$

Physical restrictions and convexity necessitate $\alpha > 0$, $\gamma < 0$ and $\delta > 0$ (David et al., 2005).

Finite Element Solution. To solve the finite element problem, we first partition the computational domain into smaller quadrilateral elements and use standard isoparametric bilinear shape functions

$$\vec{X} = N(s_1, s_2)\vec{X}^e \qquad \text{and} \qquad \vec{x} = N(s_1, s_2)\vec{x}^e \tag{3.7}$$

where the $\vec{X}^e$ and $\vec{x}^e$ are reference and deformed nodal positions, respectively. Nodal displacements are then calculated by solving the virtual work statement (3.3) on each element using a Newton-Raphson algorithm, subject to appropriate traction and displacement boundary conditions. In post-processing, the stresses are calculated at the Gauss quadrature points $s_1 = \pm 1/\sqrt{3}$, $s_2 = \pm 1/\sqrt{3}$.

Boundary Conditions. Since the anterior lens capsule is assumed to be symmetric with respect to both x and y axes (whether or not we are using radial axisymmetry), we consider only the surface in the first quadrant. There are three boundaries, $\partial\Omega^1$, $\partial\Omega^2$ and $\partial\Omega^3$ denoting the boundaries along the *yz-*, *xz-* and *xy-* planes respectively. An additional boundary $\partial\Omega^4$ will denote the edge of the capsulorhexis. The first two boundaries are free to move along their plane and are assigned a rolling displacement boundary condition, i.e.

$$u_1 = 0 \text{ on } \partial\Omega^1 \text{ and } u_2 = 0 \text{ on } \partial\Omega^2 \tag{3.8}$$

where $\vec{u} = \sum u_i \vec{e}_i$ is the nodal displacement in terms of global coordinates, and are $\vec{e}_i$ the orthonormal bases associated with this global Cartesian coordinate system. The third boundary, which corresponds to the equator of the lens capsule, may be assigned either a rolling boundary condition,

$$u_3 = 0 \text{ on } \partial\Omega^3 \tag{3.9}$$

or a fixed boundary condition

$$\vec{u} = \vec{0} \text{ on } \partial\Omega^3. \tag{3.10}$$

On the fourth (CCC) boundary, we impose a traction free boundary condition

$$\vec{T}^{(n)} = \vec{0} \text{ on } \partial\Omega^4. \tag{3.11}$$

Material Parameters. Best-fit material parameters for the Fung constitutive equation were obtained using a sub-domain inverse finite element analysis of data based on tracking the displacements of sets of five markers placed on the surface of a distended anterior lens capsule (David et al., 2005). It was shown that the anterior lens capsule exhibits regionally varying anisotropy, starting out as isotropic at the pole (i.e., Y-suture) and becoming progressively stiffer in the circumferential direction compared to the meridional direction as one moved closer to the equator. For illustrative purposes, consider an idealized material parameter profile with fixed $c = 0.02 \text{ N/mm}$, $c_3 = 1.0$ and baseline values $c_1^P = 16$ and $c_2^P = 16$ at the pole (see equation 3.4), with

$$c_1 = c_1^P(1 + 0.5arc(\vec{X})), \qquad c_2 = c_1 / 2^{arc(\vec{X})} \tag{3.12}$$

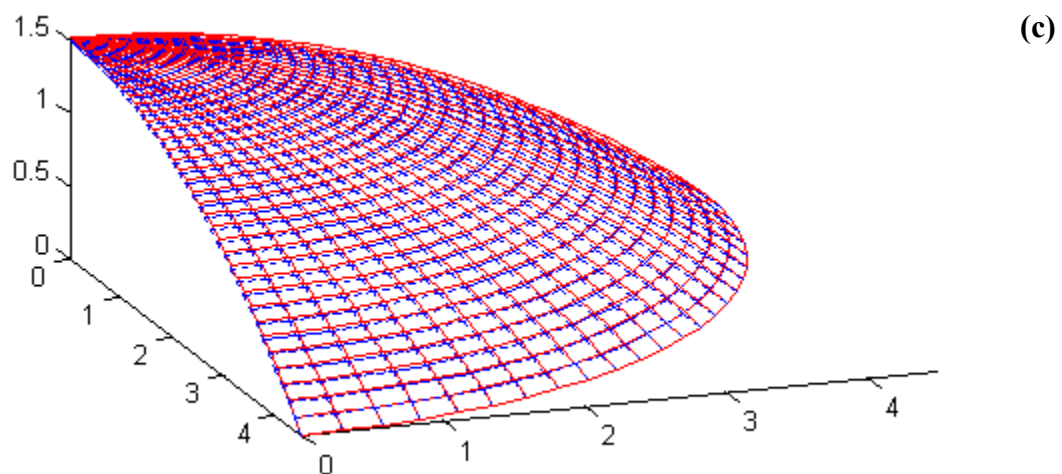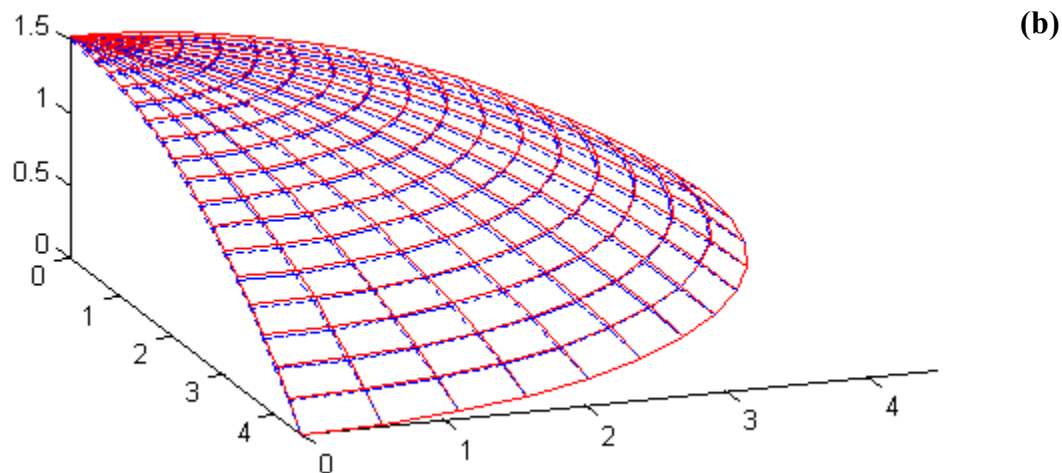where $arc(\vec{X})$ is the arclength along the surface computed from the pole to $\vec{X}$.
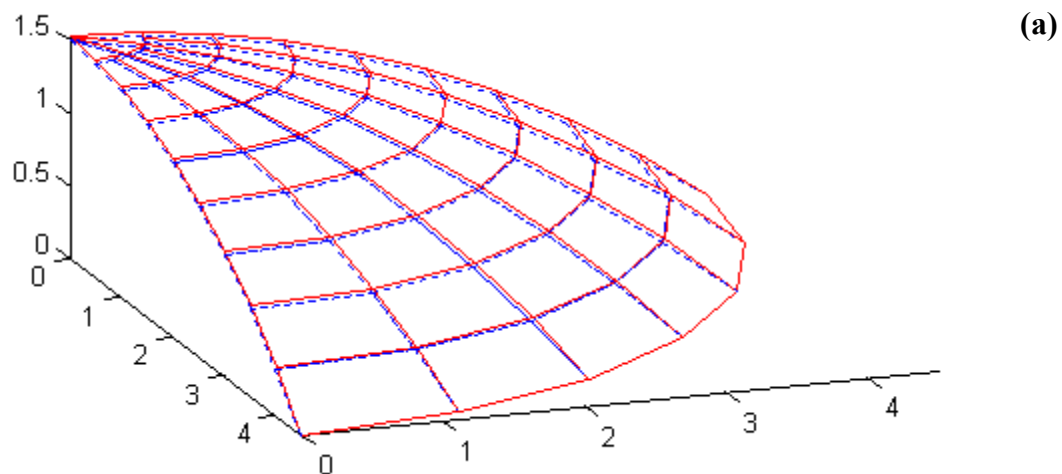
Figure 3.1. FEM surface plot for three meshes. **(a)** Coarse mesh (51 elements, approximately 9x6), **(b)** fine mesh (210 elements, approximately 18x12), and **(c)** very fine mesh (852 elements, approximately 36x24), assuming quarter-symmetry, showing both the reference (dashed) and deformed surface pressurized to 5 mmHg (solid) for an isotropic material. All dimensions in mm.
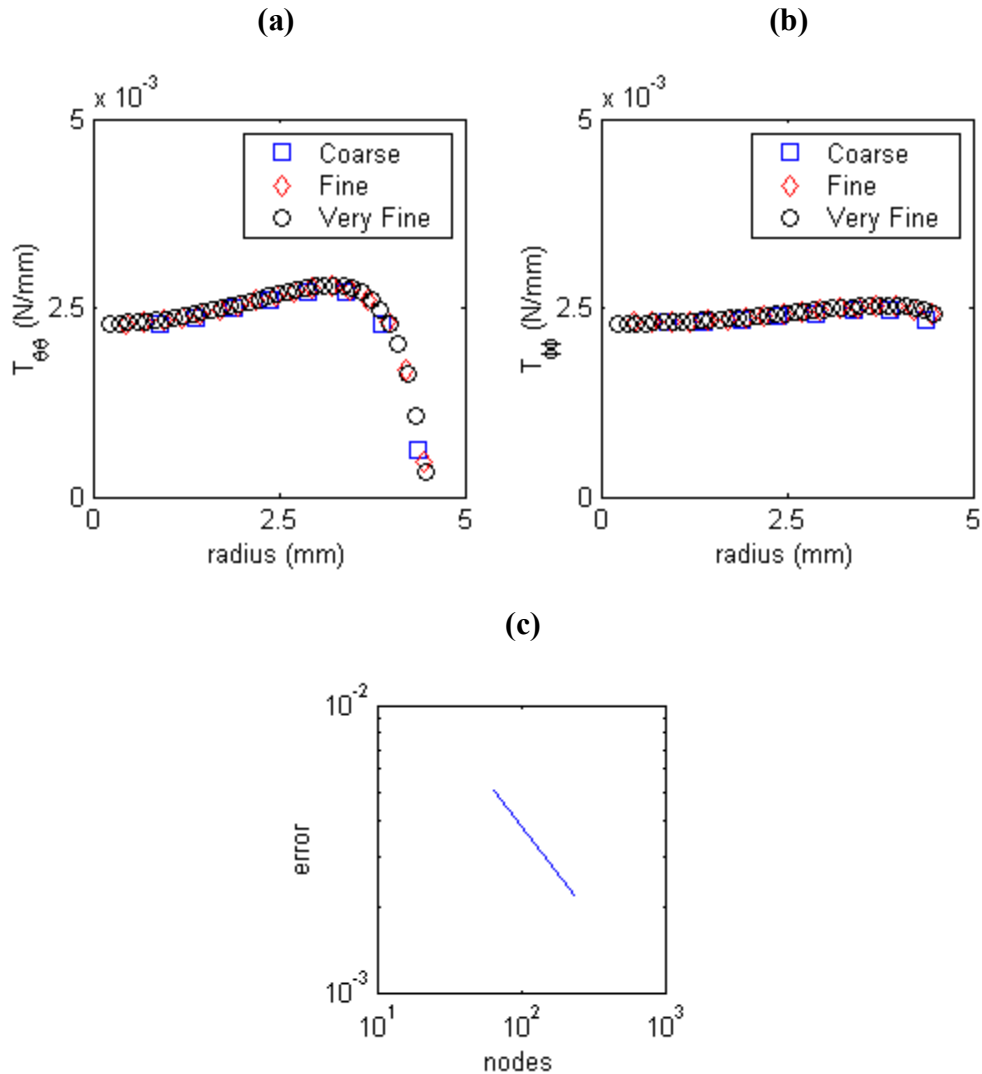
(a) **(b)**

(c)

Figure 3.2. Effects of mesh refinement. **(a)** Circumferential stresses, and **(b)** meridional stresses, computed at Gauss points, for an isotropic material based on 3 mesh densities: coarse (52 elements), fine (210) and very fine (852). The distending pressure equals 5 mmHg. **(c)** L2 error due to mesh refinement, converging at -0.646, thus indicating near quadratic convergence as expected.

Results

Finite element studies require meshes that demonstrate a reasonable degree of accuracy. Although one could always use as many elements as possible, the additional computing time may be unnecessary if coarser meshes prove adequate. To this end, we first consider a homogenous, isotropic membrane with a fixed boundary condition at the

equator. The parameter values used are $c = 0.02 \, \text{N/mm}$, $c_1 = c_2 = 16$ and $c_3 = 1.0$. The membrane is pressurized to $p = 5$ mmHg, which corresponds to the physiological pre-stress exerted by the lens on the anterior capsule (Heistand et al., 2005a). Figures 3.1a, 3.1b and 3.1c show the reference (dashed) and loaded (solid) configurations for three mesh sizes with 51 (coarse), 210 (fine) and 852 (very fine) elements respectively. Figures 3.2a and 3.2b show the calculated circumferential and meridional stresses for the three meshes. Note that the 3 meshes show nearly identical stresses, with the L_2 error converging at -0.646 (Figure 3.2c). Consequently, our subsequent calculations make use of fine meshes (210 elements), with no attempt at adaptive meshing to account for regions of strong gradients.

We next compare the isotropic membrane above with a regionally-dependent anisotropic membrane. The parameter values for the latter membrane are the same for c and c_3 everywhere, but with $c_1 = c_2 = 16$ at the pole with arc length-based variation according to (3.12). For instance, a sample material profile based on arc length intervals is given by Table 3.1.

Table 3.1. Sample material parameter profile. The profile is based on porcine lens capsule data, using the Fung model. The parameters shown are calculated from (3.12) for representative arc length values.

Arc length (mm)	0	1	2	3	4
c_1	16	24	32	40	48
c_2	16	12	8	5	3

Figure 3.3a compares the deformation profiles of the homogenous/isotropic and the regionally varying anisotropic membranes. Note that the isotropic membrane did not deform as much as the anisotropic membrane, hence a direct comparison of stresses is not presented (the other reason is that the stored energy for a given biaxial stretch is not constant throughout the anisotropic membrane, whereas it is constant for the homogenous/isotropic case; Figures 3.3b and 3.3c).
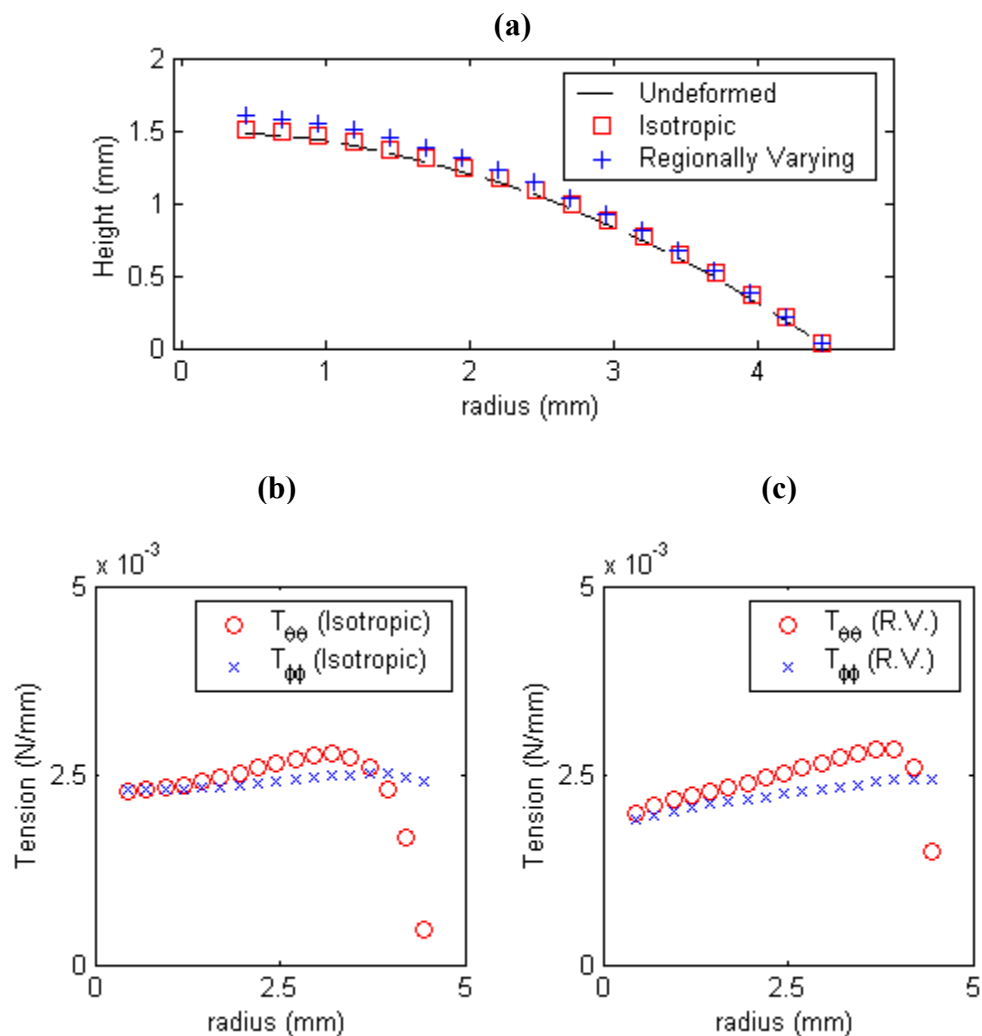

Figure 3.3 Effects of anisotropy in situ. **(a)** Deformation profile of reference (dashed) and isotropic and regionally-varying (R.V.) anisotropic materials in situ (i.e. at 5 mmHg). Circumferential and meridional tensions are shown for **(b)** isotropic and **(c)** R.V. anisotropic materials. Both material types are subject to fixed boundary conditions.
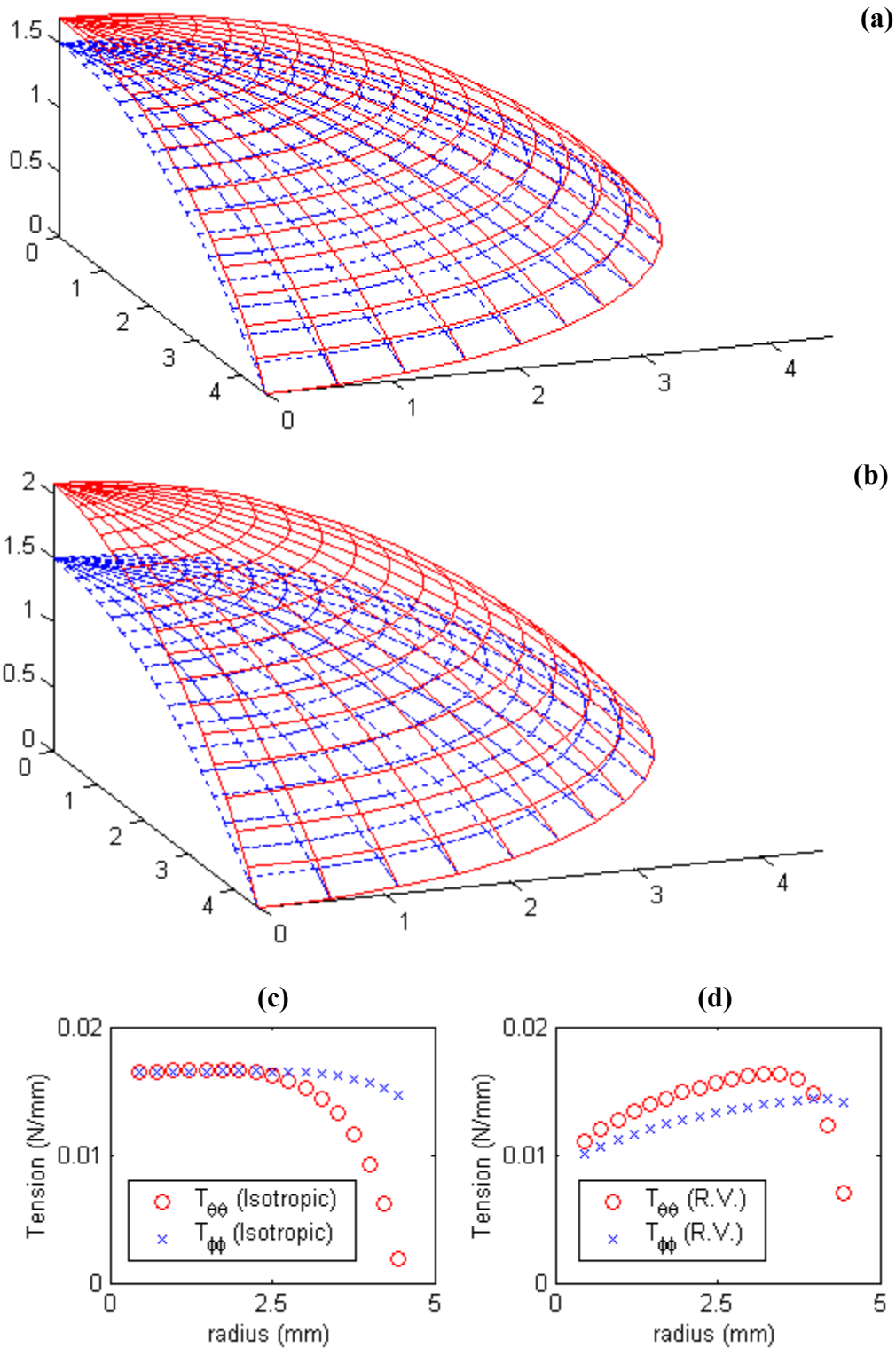
Figure 3.4. Effects of anisotropy at 35 mmHg. Surface plots of **(a)** isotropic, and **(b)** R.V. materials, showing reference (dashed) and deformed (at 35 mmHg) geometries, all dimensions in mm. Circumferential and meridional tensions are shown for **(c)** isotropic and **(d)** R.V. anisotropic materials. Both material types are subject to fixed boundary conditions.

The difference between the isotropic and anisotropic cases is more evident when the membrane is inflated to 35 mmHg, levels at which the anterior lens capsule reaches its physiologic maximum distension. The isotropic and regionally varying deformation profiles are shown in Figures 3.4a and 3.4b, respectively. Note that the height at the pole increased close to the 0.5-0.75 mm reported experimentally (Pedrigi et al., to be published). Figures 3.4c-d plot the tensions of the isotropic and anisotropic membranes at 35 mmHg.
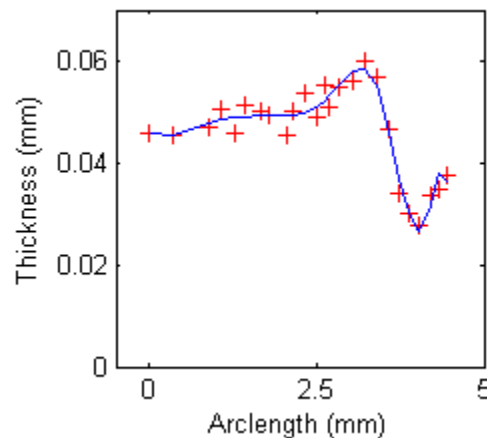

Figure 3.5. Thickness profile of the anterior lens capsule. The red (+) marks denote experimental data obtained using histology. The solid blue line plots a 10th order polynomial function used to fit the data. Arc length is measured from the pole (in mm).

Calculation of stresses requires thickness measurements of the lens capsule, which are known to vary along the meridian of the lens capsule (Burd et al, 2002). We use our own thickness measurements, based on a histological procedure, and normalized to account for drying of the sample during the experiment. A 10th order polynomial function, shown in Figure 3.5, was used to fit the data. Figures 3.6a-b show the stresses of the isotropic and anisotropic membrane at 5 mmHg, obtained post-hoc using the

tensions in Figures 3.3b-c and thickness profile. Note the flatter stress profile throughout the membrane, except at a small region near the equator.
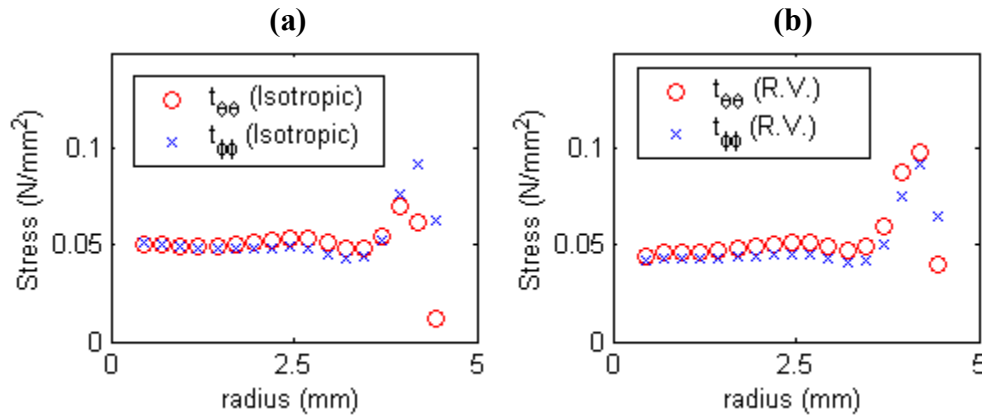

Figure 3.6. Effects of anisotropy on stress (in situ). Circumferential and meridional Cauchy stresses are shown for **(a)** isotropic and **(b)** regionally-varying (R.V.) anisotropic materials. Both materials are in situ (at 5 mmHg) and subject to fixed boundary conditions. Stresses are computed using the thickness profile in Figure 3.6.

Next, we compare the effects of fixed displacement and rolling boundary conditions at the equator, again with the membrane "pre-stressed" with 5 mmHg. Figure 3.7a shows the deformation profiles, whereas Figures 3.7b and 3.7c compare the circumferential and meridional stresses. It is interesting to note that dissimilarities in the stress responses occur only near the equator, implying that boundary effects do not affect the membrane away from that boundary, as one would expect generally. This would suggest that ophthalmologic devices, such as the haptics in intraocular lens and capsular bend rings, do not contribute significantly to stresses away from the equator. This may also be important in understanding the accommodation of the lens and the associated mechanics of the lens capsule. In addition, we observe that the regionally varying anisotropy is favorable to the geometry of the lens capsule. Whereas an isotropic membrane subjected to rolling boundary conditions at the equator tended to deform

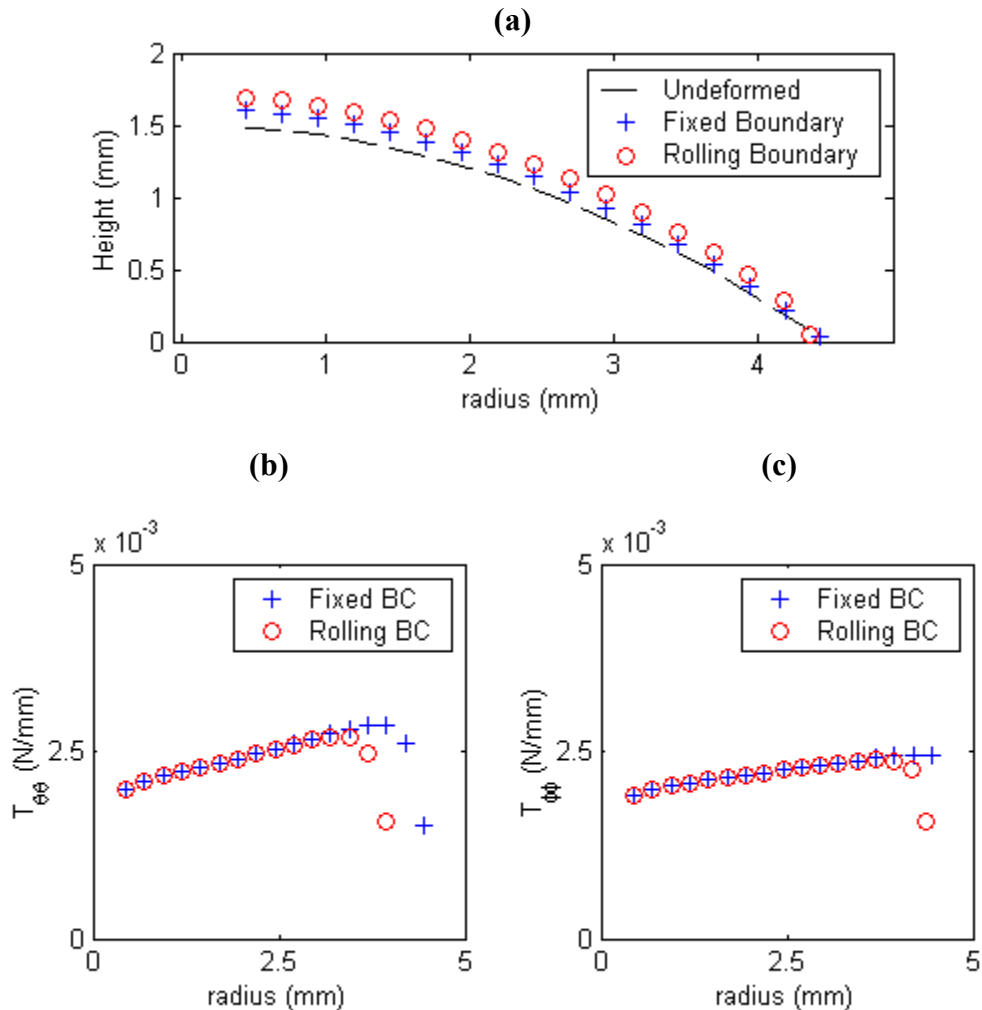closer to a sphere, the anisotropic membrane preserved its flattened shape after pressurization (not shown).

Figure 3.7. Effects of boundary conditions. **(a)** Deformation profile of reference (dashed) and regionally-varying (R.V.) anisotropic materials in situ (at 5 mmHg) subject to fixed and rolling boundary conditions. **(b)** Circumferential and **(c)** meridional tensions (at 5 mmHg) are shown for the r.v anisotropic material subject to the two boundary conditions.

Figure 3.8a shows the geometry of the lens capsule after introducing a hole of cross-sectional radius 2.5 mm, with rolling boundary conditions. Assuming hyperelasticity, we can use the deformed intact pre-stressed membrane as our initial configuration, and the deformed membrane with a hole as our final configuration. The

effect is similar to performing continuous circular capsulorhexis (CCC) on the anterior lens capsule. We note that the CCC increases the circumferential stresses (Figure 3.8b), particularly at the edge of the hole, and significantly decreases the meridional stresses (Figure 3.8c), with $T_{\phi\phi} \equiv T_{22} = 0$, along the edge of the hole, as it should to satisfy the traction-free boundary condition.
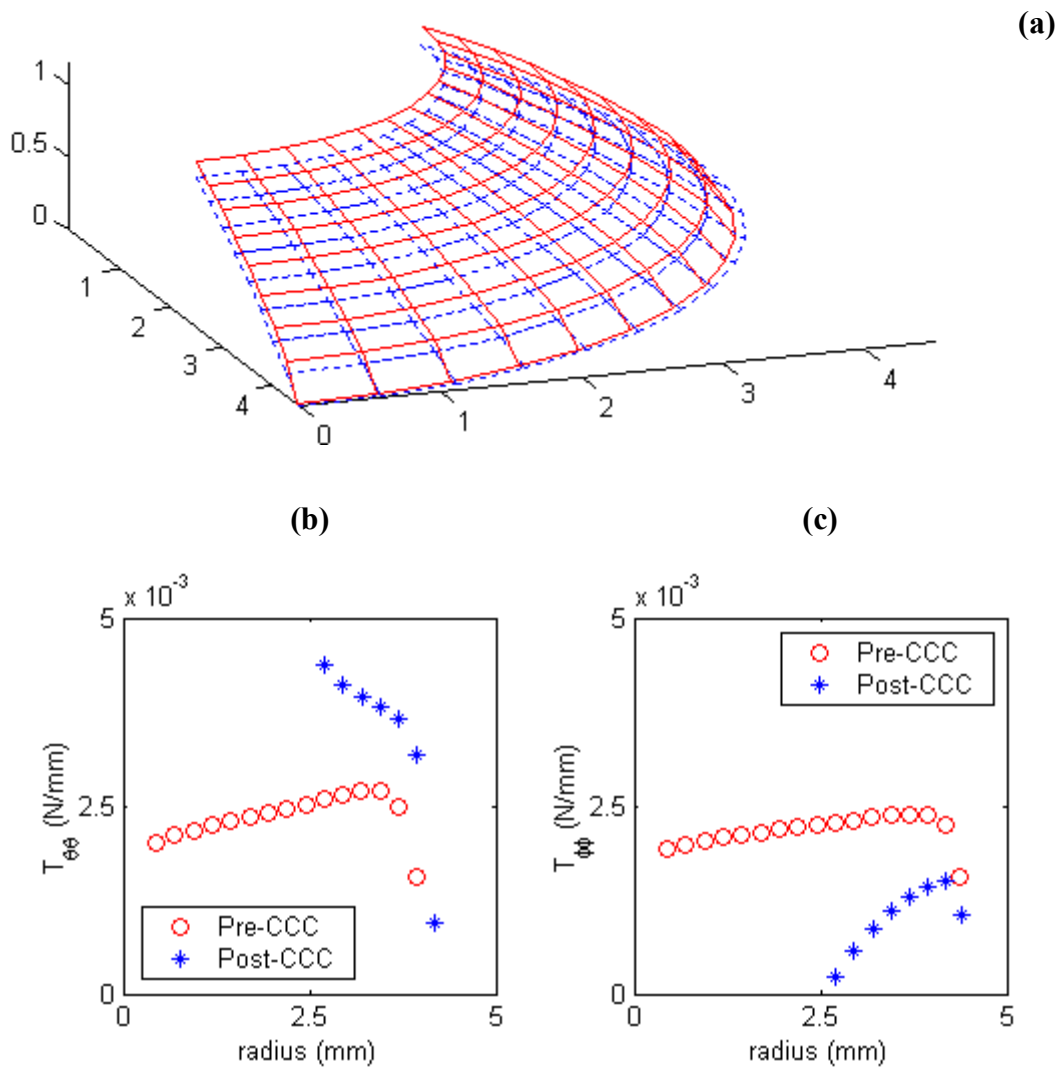
Figure 3.8. Effects of capsulorhexis (CCC). **(a)** Surface plot showing regionally-varying (R.V) anisotropic material with a hole of radius 2.5 mm at reference (dashed) and in situ, all dimensions in mm. **(b)** Circumferential and **(c)** meridional tensions are shown for the R.V. anisotropic material without the hole (pre-CCC), and with the hole (post-CCC). Both are in situ (at 5 mmHg) and subject to rolling boundary conditions.
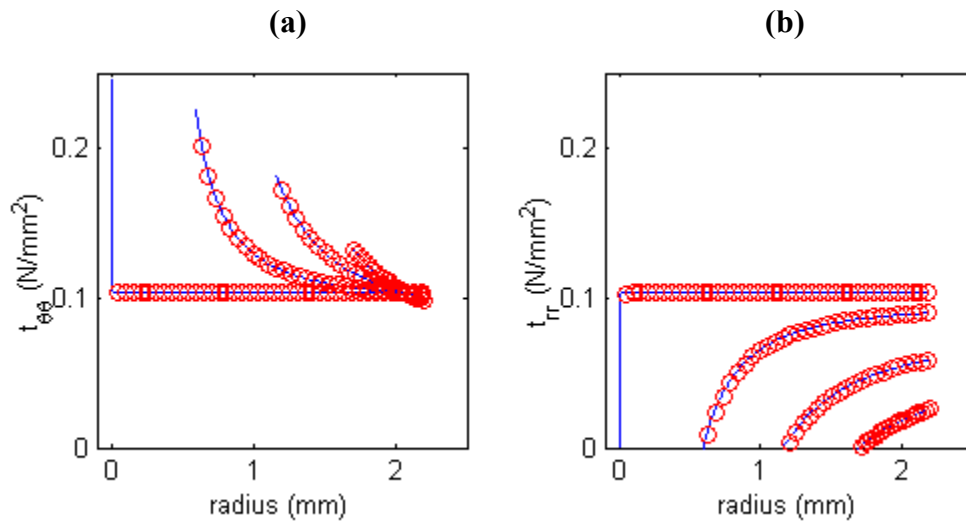
Figure 3.9. FEM patch test using flat circular sheet. **(a)** Circumferential and **(b)** radial stresses for 4 different flat circular sheets with 4 hole sizes, prestretched 10% at the outer edge and unpressurized (circles). Results are for 40 elements maximum along a meridional line. The solid lines depict the corresponding results via the strong form (analytic) solution (David and Humphrey, 2004).
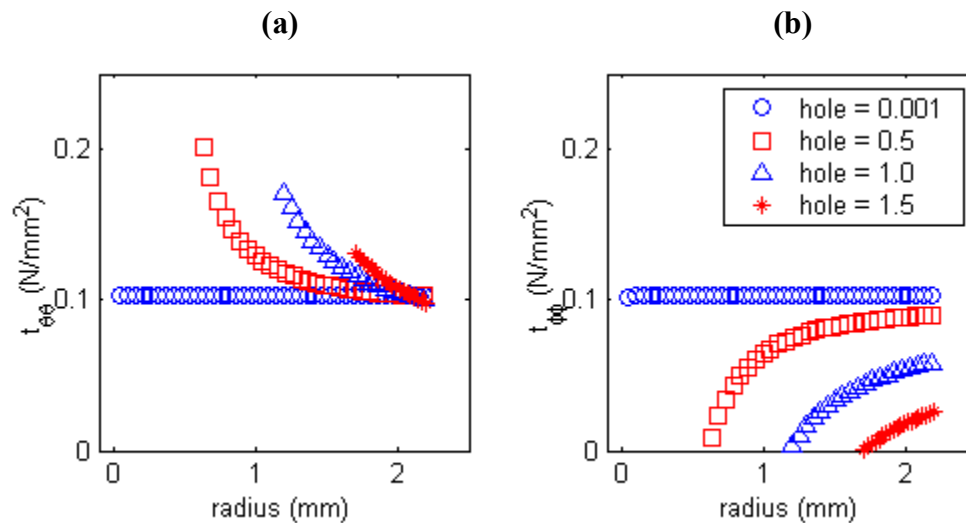
Figure 3.10. Patch test using circular sheet at 5 mmHg. **(a)** Circumferential and **(b)** meridional stresses for 4 different flat circular sheets with 4 hole sizes, prestretched 10% at the outer edge and pressurized to 5 mmHg.

Lastly, we perform a simple finite element (i.e. weak form solution) inflation of a flat, circular membrane with a hole. This provides a direct comparison with a strong form patch test that stretched a flat circular membrane with different anisotropies (David and

Humphrey, 2004). In that study, computations were presented for a circular membrane with an outer radius of 2.0 mm and varying hole sizes of 0.001 mm, 0.50 mm, 1.0 mm and 1.5 mm. The material parameters used were fixed $c = 0.5$ N/mm^2, $c_3 = 0.05$ and $c_1 = c_2 = 0.75$ for the isotropic case. Using the same values here, the membrane was not pressurized (hence it remained flat), but was stretched by 10% at the outer boundary. Moreover, the stress resultants obtained here are converted to stresses by multiplying by the out-of-plane thinning, assuming incompressibility. The results of the finite element solution agreed exactly with the analytical solution (Figures 3.9a and b). Of course, because of the uniform mesh size used, the current finite element solution did not capture the steep stress gradient effects in the limiting case of a pin-hole (i.e. inner radius = 0.001 mm) that was predicted by the analytical solution (refer to figures in David and Humphrey, 2004). Such a solution does not apply to the problem of a CCC, however. In Figures 3.10a-b, we show the same extended flat membrane, but pressurized to 5 mmHg. Note that the stress responses are virtually identical to that of the extended flat membrane.

Discussion

It has been known for some time that (see Krag et al., 1994), similar to other soft tissues, the lens capsule exhibits a highly nonlinear material behavior. Moreover, it is now known (Heistand et al., 2005b) that the porcine lens capsule is under a significant pre-strain under normal conditions (10-12% biaxially). Consequently, any analysis of the biomechanics should be based on a fully nonlinear approach. Although suitable finite element methods have long been available for nonlinear membranes (e.g., Oden, 1972), there was a pressing need for better information on the material properties of the lens

capsule. Using a new experimental approach and a custom sub-domain inverse finite element method, we recently found a strong regional variation in the anisotropy of the porcine anterior lens capsule (Chapter II). As revealed by Figure 3.6, this regional variation appears to yield a nearly uniform and nearly equibiaxial stress field across the lens capsule. If so, this is consistent with findings for other soft tissues. For example, Humphrey (2003) showed that current predictions suggest that residual stresses, muscle tone, and regional properties work together to yield a uniform transmural stress in arteries in normalcy. Mounting evidence thus seems to suggest that cells may tend to organize matrix locally to affect the global state of stress. If indeed the cells seek to establish an "optimal" state of stress (or strain) everywhere, Figure 3.8 suggests that a CCC greatly perturbs the stress field from this optimal. As expected, introducing a hole into a pre-strained membrane will relieve some of the pre-stresses—in the case of the anterior lens capsule, this results in a meridional retraction and circumferential expansion. It would be of great interest to use concepts of tissue growth and remodeling (e.g. Humphrey and Rajagopal, 2002) to study possible ways in which this perturbed stress field could possibly be returned towards normalcy, given the constraint of course of the traction-free edge at the CCC. Indeed, given the known cellular response to cataract surgery—migration of lens epithelial cells from the anterior to the posterior capsule, where they exhibit a wound healing like response—one wonders if the perturbation is too severe to be overcome naturally. This may be analogous to the ability of fibroblasts to heal small dermal wounds (Tranquillo and Murray, 1992) whereas large wounds will heal only with clinical interventions, including suturing and antibiotics.

Although the complex material behavior was modeled reasonably well, there is a need for further improvement of the model. First, there is a need to relax the axisymmetry and to model the slightly ellipsoidal shape with an improved surface fit. Second, there is a need to address the boundary conditions at the equator, particularly as it relates to accommodation. Toward this end, there is a pressing need for better information on the biomechanics of the ciliary process. Whereas porcine eyes do not accommodate, this is one of the most important issues in human ophthalmology. Figure 3.7 reveals that relaxing a fixed displacement boundary condition along the equator has a significant effect on the stresses near the boundary but very little effect away from the boundary. Understanding this may influence the design of intraocular lens haptics and capsular tension rings in the future. Another possible implication of this boundary effect is that although accommodation may alter the geometry of the anterior lens capsule, it may leave the stresses unchanged near the pole (Y-suture).

In conclusion, our preliminary finite element models and studies suggest that the inherent regionally varying anisotropy of the lens capsule serves to reduce the stresses on the membrane as well as preserve its simple geometry. We also showed that boundary conditions at the equator had little effect on the stresses away from the equator. Lastly, our model of the CCC showed that the capsulorhexis induced significant changes in the stresses of the lens capsule. Further improvements in our model are desired in order to better understand the biomechanics involved in capsulotomy and other surgical procedures performed on the human lens capsule.

CHAPTER IV

REDISTRIBUTION OF STRESS DUE TO A CIRCULAR HOLE IN A NONLINEAR ANISOTROPIC MEMBRANE[1]

Overview

Many clinical procedures introduce holes into thin tissues that are typically under multiaxial stresses and finite strains. Such incisions change the stresses and strains from their homeostatic values, which may induce cells to alter their orientation and cytoskeletal organization as well as to migrate, proliferate, change their synthesis of matrix, or even to enter the cell death cycle. To correlate such changes in cellular activity with changes in the mechanics, we need solutions for the native and the perturbed boundary value problems. Such problems will often be complex and require a finite element solution; weak solutions should be evaluated independently, however, at least for special cases. Herein, we present a numerical solution of the governing nonlinear ordinary differential equation for the special case of stress redistribution due to the introduction of a circular hole into a finitely deformed, Fung-type, circular membrane that exhibits a cylindrical orthotropy. Among other results, we show that the anisotropy plays an increasingly greater role as the size of the hole becomes smaller, which is of course a goal of minimally invasive procedures.

Introduction

Many cell-types respond to changes in their mechanical environment; such cells are collectively called mechanocytes, which include chondrocytes, endothelial cells, epithelial cells, fibroblasts, macrophages, myocytes, and osteoblasts. Indeed, it appears that, via processes during development as well as normal growth and remodeling, cells and thus tissues tend to organize so as to achieve a preferred (perhaps optimal) state of stress or strain (Cowin, 2000). Disease, injury, and clinical intervention commonly perturb these homeostatic stress and strain fields, often by inducing significant gradients therein. Examples in the vasculature include hypertension, the formation of intracranial aneurysms, and balloon angioplasty (Humphrey, 2002). Herein, however, our interest is on immediate changes in the stress and strain fields of membranes due to the surgical or traumatic introduction of a circular hole. Whereas Rivlin and Thomas (1951) considered a related problem for isotropic membranes (see, too, Verma and Rana, 1978; Varley and Cumberbatch, 1980), we study for the first time the role of anisotropy in the redistribution of stress due to a circular hole in a prestretched circular membrane that is initially subject to an equibiaxial state of stress. Although not intended to address a particular clinical procedure, such results may provide insight into the analysis of early mechanotransduction mechanisms related to needle sticks, skin biopsies, percutaneous catherization, laparoscopic surgery, cataract surgery, and similar clinical procedures (see Tranquillo and Murray, 1992). Moreover, these results will serve as important patch tests for guiding the development of fully nonlinear finite element models that can address more complex geometries and boundary conditions.

Methods

Theoretical Framework. We consider elastic responses if isotropic or cylindrically orthotropic membranes, thus the introduction of a circular hole into an equibiaxially prestretched membrane is equivalent to the stretching of a membrane containing a central hole. Hence, consider a thin circular membrane having a central circular hole and be subjected to a uniform radial traction on its outer circumference. Using cylindrical coordinates, we map the position of a material particle originally at (R,Θ) to (r,θ) following the application of loads; moreover we denote the outer and inner undeformed radii by R_o and R_i and the outer and inner deformed radii by r_o and r_i respectively. Thus, a motion of the form:

$$r = r(R), \quad \theta = \Theta, \tag{4.1}$$

yields the following components of the deformation gradient:

$$\mathrm{F} = \begin{bmatrix} \lambda_R & 0 \\ 0 & \lambda_\Theta \end{bmatrix} = \begin{bmatrix} r' & 0 \\ 0 & \dfrac{r}{R} \end{bmatrix}, \tag{4.2}$$

wherein λ_i are principal stretch ratios and the prime denotes differentiation with respect to R. The Green strain is

$$\mathbf{E} \equiv \begin{bmatrix} E_{RR} & 0 \\ 0 & E_{\Theta\Theta} \end{bmatrix} = \begin{bmatrix} \lambda_R & 0 \\ 0 & \lambda_\Theta \end{bmatrix}. \tag{4.3}$$

The mechanical behavior of many biomembranes is describable via a Fung-type exponential pseudostrain-energy function W (Fung, 1990; Humphrey, 2002):

$$W = \tfrac{1}{2}c(e^Q - 1), \tag{4.4}$$

where c is a material parameter having units of stress and

$$Q = c_1 E_{RR}^2 + c_2 E_{\Theta\Theta}^2 + 2c_3 E_{RR} E_{\Theta\Theta} \tag{4.5}$$

where the c_i are nondimensional material parameters. The Cauchy stress $\mathbf{t}$ is given by (Humphrey, 2002):

$$\mathbf{t} = \frac{\mathbf{T}}{h} = \frac{1}{h}\left(\frac{1}{\det \mathbf{F}}\right)\mathbf{F} \cdot \frac{\partial(WH)}{\partial \mathbf{E}} \cdot \mathbf{F}^{\mathrm{T}} = \mathbf{F} \cdot \frac{\partial W}{\partial \mathbf{E}} \cdot \mathbf{F}^{\mathrm{T}}, \tag{4.6}$$

where $\mathbf{T}$ is a stress resultant and h is the deformed thickness ($h = \lambda_Z H$ where H is the deformed thickness and $\lambda_Z = 1/\lambda_R \lambda_\Theta$ if the membrane is incompressible. The nonzero components of stress are thus,

$$t_{rr} = \lambda_R^2 \frac{\partial W}{\partial E_{RR}}, \quad t_{\theta\theta} = \lambda_\Theta^2 \frac{\partial W}{\partial E_{\Theta\Theta}}, \tag{4.7}$$

and the only non-zero equilibrium equation is

$$\frac{\partial t_{rr}}{\partial r} + \frac{1}{r}\left(t_{rr} - t_{\theta\theta}\right) = 0. \tag{4.8}$$

Note, therefore, that for the motion in Eq. (4.1),

$$\frac{dt_{rr}}{dR} = \frac{\partial t_{rr}}{\partial r}\frac{\partial r}{\partial R} + \frac{\partial t_{rr}}{\partial \theta}\frac{\partial \theta}{\partial R} = \lambda_R \frac{\partial t_{rr}}{\partial r} \tag{4.9}$$

and

$$\frac{dt_{rr}}{dR} = \frac{\partial t_{rr}}{\partial \lambda_R}\frac{\partial \lambda_R}{\partial R} + \frac{\partial t_{rr}}{\partial \lambda_\Theta}\frac{\partial \lambda_\Theta}{\partial R}. \tag{4.10}$$

Using equation (4.2), we rewrite the following partial derivatives::

$$\frac{\partial \lambda_R}{\partial R} = r'', \qquad \frac{\partial \lambda_\Theta}{\partial R} = \frac{1}{R}\left(\lambda_R - \lambda_\Theta\right). \tag{4.11}$$

Thus, from equations (4.8) to (4.11), the radial equilibrium equations can be written as a second-order nonlinear ordinary differential equation for $r(R)$:

$$r'' = \frac{(t_{\theta\theta} - t_{rr})\frac{\lambda_R}{r} + \frac{\partial t_{rr}}{\partial \lambda_\Theta}(\lambda_\Theta - \lambda_R)\frac{1}{R}}{\frac{\partial t_{rr}}{\partial \lambda_R}} \tag{4.12}$$

Note that the exponentials cancel throughout and the right-hand side reduces to a rational polynomial in R, r and r'. In this way, the governing equation can be written in terms of a system of two first order equations. Specifically, denoting $y_1 = r$ and $y_2 = r'$, we obtain the system

$$\frac{dy_1}{dR} = y_2 = r', \quad \frac{dy_2}{dR} = r''. \tag{4.13}$$

Conditions at the inner and outer radii give rise to the two requisite boundary conditions. The inner boundary is traction-free whereas the outer boundary condition can be written as either a displacement or a traction condition. For example, let t_o be the radial stress on the outer boundary, thus

$$t_{rr}(R_o) = t_o = \lambda_R^2(R_o)\frac{\partial W}{\partial E_{RR}}\bigg|_{R_O} \tag{4.14}$$

whereas the traction-free condition at the inner boundary requires that

$$t_{rr}(R_i) = 0 = \lambda_R^2(R_i)\frac{\partial W}{\partial E_{RR}}\bigg|_{R_i}. \tag{4.15}$$

Equation (4.15) reduces to

$$\frac{dr}{dR}\bigg|_{R_i} = \sqrt{1 - \frac{c_3}{c_1}\left(\frac{r_i^2}{R_i^2} - 1\right)} \tag{4.16}$$

Numerical Method. System (4.13) is easily solved numerically. We use a shooting method to convert the boundary value problem into an initial value problem. For example, if we prescribe the deformed outer radius, then we need to find the

corresponding ("initial") values of the deformed inner radius and its derivative. Because equation (4.16) allows us to solve one of these quantities given the other, we only need to guess (i.e. find) the deformed inner radius. Let $g : a \mapsto g(a)$ be a mapping that associates a trial deformed inner radius a to a deformed outer radius $g(a)$, obtained via the numerical solution. We seek a such that $g(a) = r_o$ (given). Because r' from incompressibility, r is monotonically increasing (at each equilibria) and the mapping g is one to one. Because $g(R_i) \leq r_o$ whenever $R_o \leq r_o$ (i.e. provided we are stretching the membrane), an initial lower estimate of R_i is used for the deformed inner radius. We restrict the model to biologically reasonable stretches; hence the initial upper estimate is set at or less than $3R_i$. We then apply a bisection method until we obtain a solution within a desired tolerance, e.g. 10^{-3} as used in the actual simulations.

Illustrative Cases. It is often expedient to present general results in nondimensional form. Hence, consider a circular membrane with an initial outer radius of 2 a.u. (arbitrary units) and an initial hole of radius 0.001, 0.5, 1.0, or 1.5 a.u. Let the membrane be stretched 5%, 10%, 15%, 20% or 25% relative to the outer radius, and be endowed with isotropic ($c_1 = c_2$), radially stiffer ($c_1 > c_2$), or circumferentially stiffer ($c_1 < c_2$) behavior while fixing the stored energy of the system (i.e. $W(\lambda_R, \lambda_\Theta) = constant$ at any $\lambda_R = \lambda_\Theta$ regardless of the material symmetry). For purposes of illustration, let 'baseline' values of the parameters be: $c_1 = 0.75$, $c_2 = 0.75$, and $c_3 = 0.05$ with stress nondimensionalized by c.
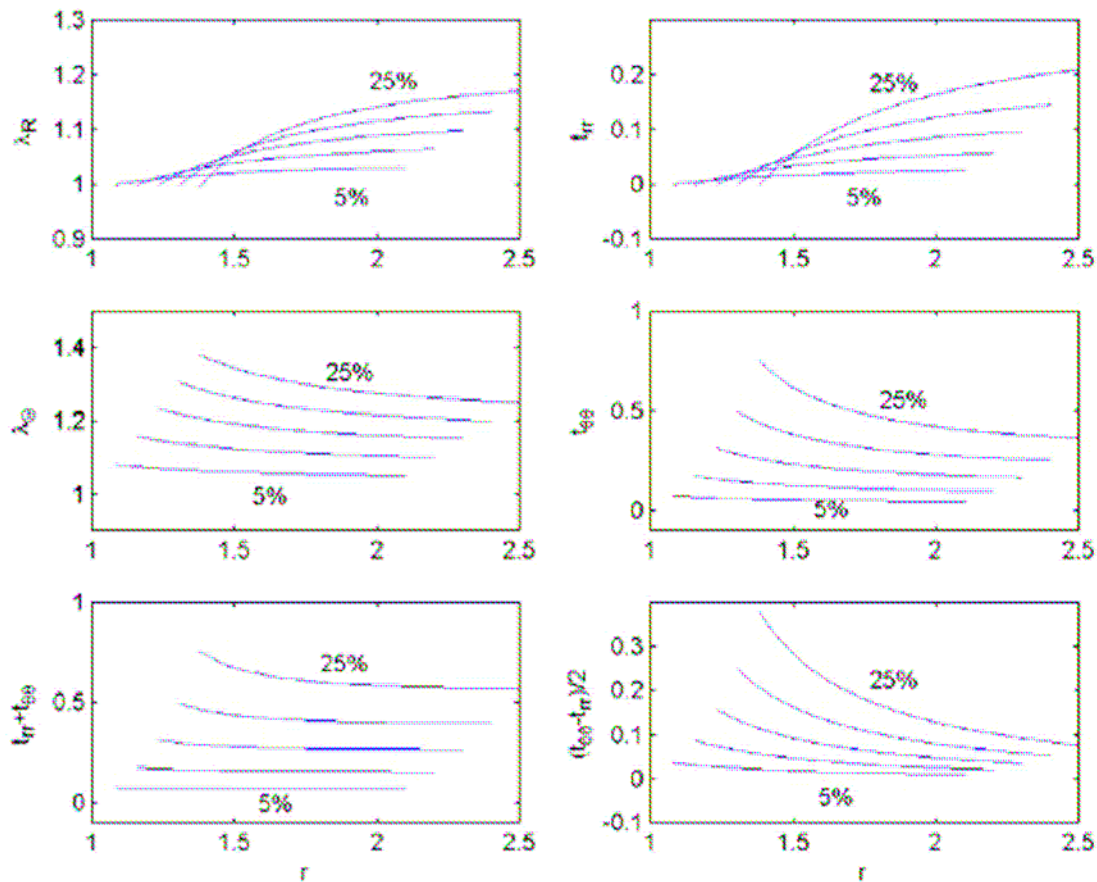
Figure 4.1. Isotropic membrane subject to 5 different stretches. Results for a membrane with undeformed hole radius of 1.0 and outer radius of 2.0 stretched by 5%, 10%, 15%, 20% and 25%. The parameters are $c_1 = 0.75$, $c_2 = 0.75$ and $c_3 = 0.05$ (isotropic case).

Results

Results for the isotropic case, with a hole of initial radius 1.0 a.u., and 5 % to 25% extensions prescribed at the outer boundary, were qualitatively similar to those obtained by Varley and Cumberbatch (1980) and others (Figure 4.1). Consistent with the monotonically decreasing circumferential stretch (middle left), the circumferential stress also decreases monotonically (middle right), with increased gradients in the inner regions as the membrane was stretched further. Conversely, the radial stress (upper right) increased monotonically from zero at the inner boundary, as required by boundary conditions, again with the largest gradients in the inner regions. Because the stress field is

principal with respect to (r, θ), the maximum in-plane stress is given by $(t_{\theta\theta} - t_{rr})/2$, which was monotonically decreasing (bottom right). The first invariant of stress, $t_{rr} + t_{\theta\theta}$, tends to be the closer to uniform across the membrane, albeit with a slight gradient in the inner region at the higher stretches (bottom left).
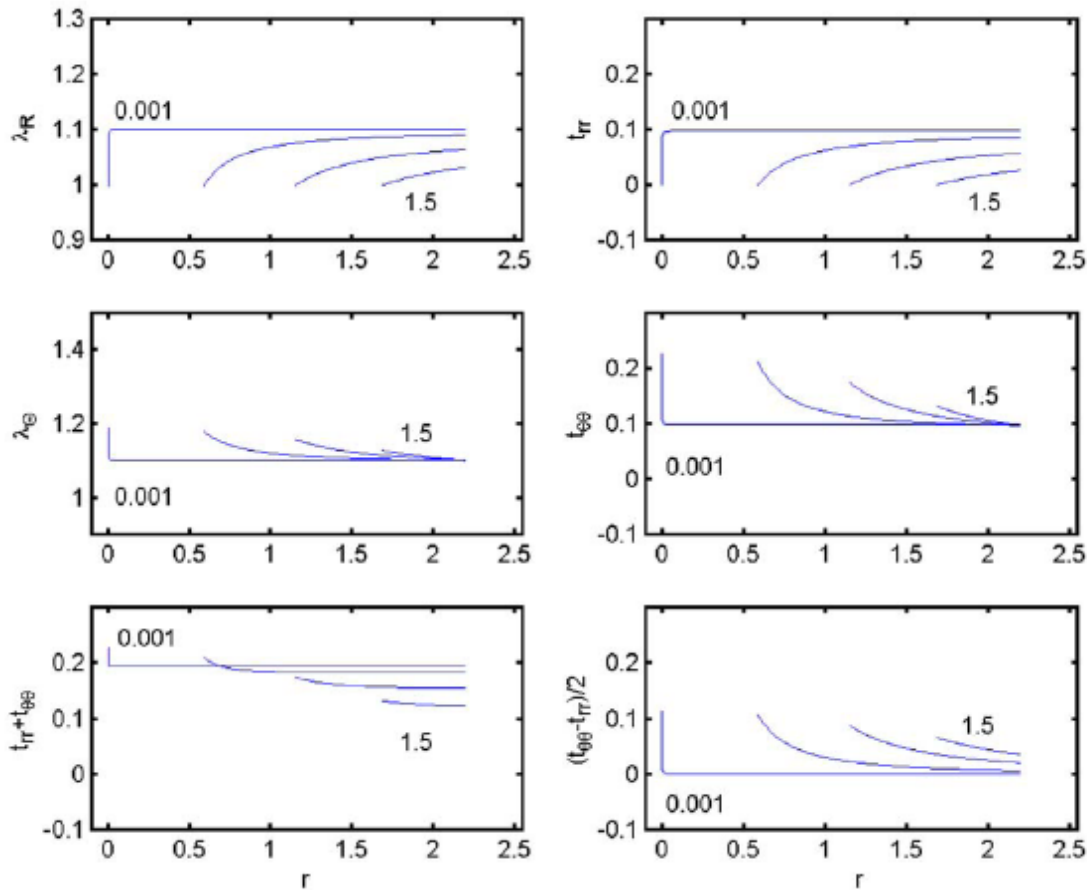
Figure 4.2. Isotropic membranes with 4 hole sizes. Four membranes with undeformed hole radii of 0.001, 0.5, 1.0 and 1.5 and an outer radius of 2.0 stretched by 10%. The parameters are $c_1 = 0.75$, $c_2 = 0.75$ and $c_3 = 0.05$ (isotropic case).

Although not shown, two anisotropic cases were considered for the same size hole and extensions at the outer boundary: first with parameters $c_1 = 0.5$, $c_2 = 1.0$ (with c_3 the same), and second, with parameters $c_1 = 1.0$ and $c_2 = 0.5$ (with c_3 the same). Both anisotropic cases produced results similar to those for the isotropic case, with only slight

differences in the values and gradients—stresses were slightly higher with $c_1 < c_2$ and lower with $c_1 > c_2$. The three cases showed notable differences in the out-of-plane thinning, however, as discussed below (Figure 4.5).

Figure 4.3. Circumferentially stiffer membranes with 4 hole sizes. Membranes and stretch are the same as Fig 4.2, but with parameters $c_1 = 0.5$, $c_2 = 1.0$ and $c_3 = 0.05$ (circumferentially stiffer case).

Results for different sized holes (initial radii of 0.001, 0.5, 1.0 and 1.5 a.u.) in an isotropic membrane extended 10% were similar as expected (Fig. 4.2). A "pinhole" resulted in a marked stress concentration but an otherwise nearly homogenous equibiaxial stress field similar to that expected in the absence of a hole (wherein $(t_{\theta\theta} - t_{rr})/2$, the in-plane stretch, at all r). An increase in the size of the hole decreased the maximum value

of the circumferential stress and its gradient; indeed, in the limit as the radius of the hole approaches the outer radius, a nearly homogenous stress is imagined consistent with a thin-ring approximation. Results are similar for the different components of stress and strain.
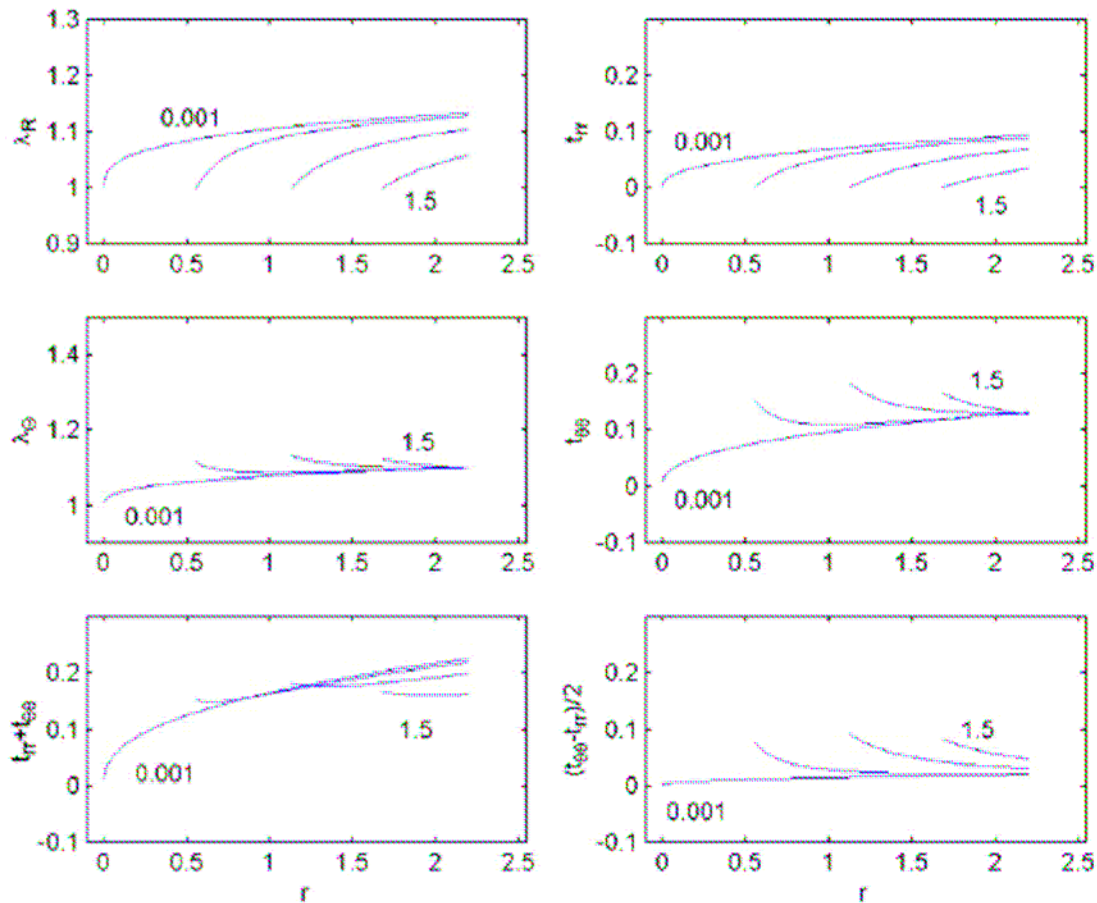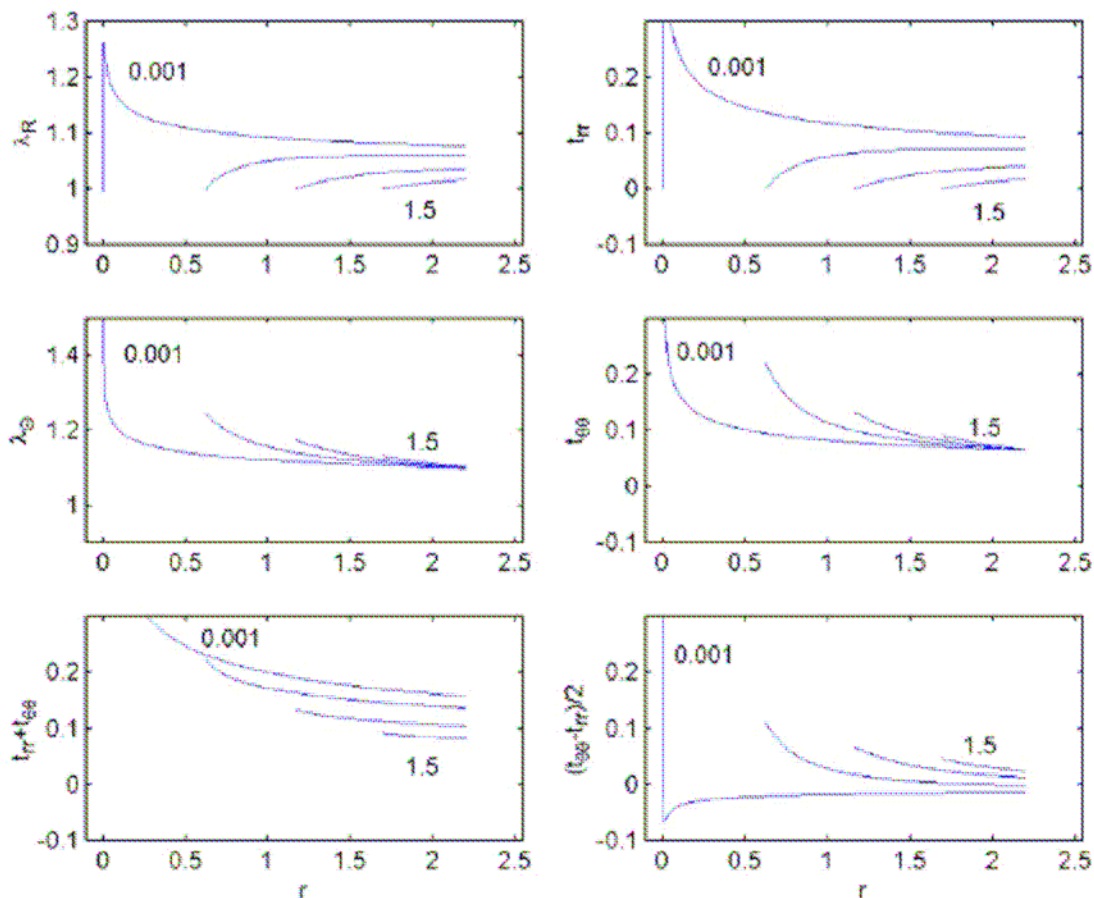

Figure 4.4. Radially stiffer membranes with 4 hole sizes. Membranes and stretch are the same as Fig 4.2, but with parameters $c_1 = 1.0$, $c_2 = 0.5$ and $c_3 = 0.05$ (radially stiffer case).

In contrast to the isotropic results, both anisotropies (radially vs. circumferentially stiffer) yielded significantly different distributions of stress and stretch as the hole became smaller. In particular, in the pinhole case, the circumferentially stiffer membrane had much lower stresses near the hole (Fig. 4.3), whereas the radially stiffer membrane

had much higher stresses and gradients near the hole (Fig. 4.4). As the size of the hole increased, anisotropic cases yielded more comparable stress patterns although $t_{\theta\theta}$ was typically higher in the circumferentially stiffer case and lower in the radially stiffer case. Note, too, the very different distributions of the maximum shear stresses (cf. lower right panels in Figs. 4.2-4). These findings seem to suggest that the anisotropy becomes very important when the hole size is small compared to the overall size of the membrane.
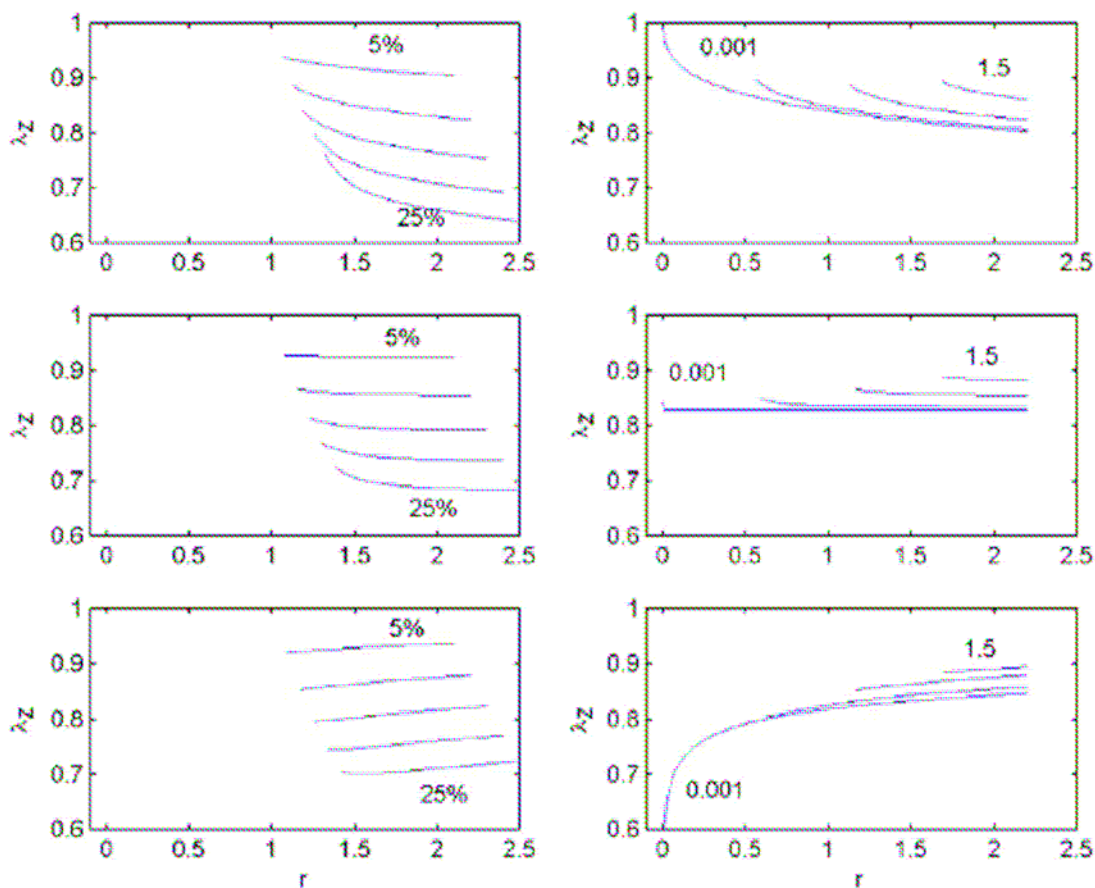
Figure 4.5. Out of plane thinning for 3 material types. The panels on the left show out-of-plane thinning for membranes with an undeformed hole radius of 1.0 and undeformed outer radius of 2.0 stretched to 5%, 10%, 15%, 20%, and 25%; the top panel is for the circumferentially stiffer case ($c_1 = 0.5$, $c_2 = 1.0$), the middle panel is for the isotropic case ($c_1 = 0.75$, $c_2 = 0.75$) and the bottom panel is for the radially stiffer case ($c_1 = 1.0$, $c_2 = 0.5$). The panels on the right show out-of-plane thinning for membranes with an undeformed hole radii of 0.001, 0.5, 1.0 and 1.5, and undeformed outer radius of 2.0 stretched by 10%. The top panel is for the circumferentially stiffer case, the middle panel is for the isotropic case and the bottom panel is for the radially stiffer case.

The out-of-plane thinning (Figure 4.5) was computed locally in post processing assuming incompressibility. In the isotropic case (middle two panels), the thinning was fairly uniform although slightly greater towards the outer radius in general. Note the near homogenous thinning in the pinhole case (middle right). The circumferentially stiffer case (upper two panels) revealed a monotonic thinning that was greatest near the outer radius. In contrast, the radially stiffer case (bottom two panels) revealed the greatest thinning near the inner radius. In all cases, the thinning increased as the stretch increased, and the membrane with the smaller hole had greater thinning that the one with a larger hole, as expected.

Discussion

Results from isotropic linear elasticity reveal that introducing a circular hole into a planar material under a uniform, equibiaxial stress results in a stress concentration factor $k \equiv t_{\theta\theta}(r_i)/t_o$ equal to 2.0. Given that it has long been known in isotropic finite elasticity that large deformations increase k further (e.g. from 2 to 7 for λ_Θ from ~1 to 2.5 in a Mooney-Rivlin material; Oden 1972), it is remarkable that there have been no fully nonlinear analyses in biomechanics of the role of tissue anisotropy. Herein, we considered one special case: a cylindrical orthotropy of a Fung-elastic material wherein either the radial or circumferential direction was about two times stiffer. Somewhat unexpectedly, we found that, in comparison to the isotropic case, a radially stiffer behavior can exacerbate the stress concentration whereas a circumferentially stiffer behavior can minimize it. Moreover, the role of the anisotropy is greater for the smaller holes. It is interesting in this regard that minimally invasive surgery seeks to reduce the size of the incision.

We considered but a few different anisotropies, and assumed uniform rather than regionally different anisotropies. Ryan and Humphrey (1999) showed, however, that inflated membranes such as saccular aneurysms may have regionally varying symmetries. There is clearly a need to investigate further the effects of such symmetries on stress redistribution due to the introduction of circular as well as elliptical holes. Such studies will likely require finite elements, which is beyond the present scope. We reiterate, however, that the present results are not only instructive, they can serve as important patch tests for future finite element studies, particularly for clinical situations.

In the introduction, we noted that many different clinical procedures could be considered within the context of the boundary value problem studied here, including skin biopsies, laparoscopic procedures, and cataract surgery. Indeed, as medicine and surgery move more and more towards minimally invasive procedures, small access incisions will become more common. Cataract surgery, for example, is the most commonly performed procedure in the U.S., at roughly 1.5 million operations per year (Foster, 1999). Briefly, the surgeon introduces a small circular hole in the anterior surface of the lens capsule to extract the 'clouded lens' and to implant an intraocular device. Albeit a very successful procedure, a post-surgical complication is the clouding of the intact posterior lens capsule--a complication that may be due to unnatural mechanosensitive responses by the capsular epithelial cells in response to the surgically altered stress or strain field. Such possibilities in this and similar clinical situations can only be studied if we quantify the native and perturbed stress and strain fields using fully nonlinear analyses that account for material symmetry. The present study is a first step in that direction, one that reveals

qualitative changes in a simple case that can serve as a guide (e.g. patch test) for future, more sophisticated finite element solutions.

CHAPTER V

FURTHER EVIDENCE FOR THE DYNAMIC STABILITY

OF INTRACRANIAL SACCULAR ANEURYSMS[2]

Overview

It has long been thought that intracranial saccular aneurysms enlarge and rupture because of mechanical instabilities. Recent nonlinear analyses suggest, however, that at least certain sub-classes of aneurysms do not exhibit quasi-static limit point instabilities or dynamic instabilities in response to periodic loading, and consequently, that the natural history of these lesions is likely governed by growth and remodeling processes. In this paper, we present additional results that support the finding that one particular sub-class of saccular aneurysms is dynamically stable. Specifically, we extended recent results of Shah and Humphrey, which are based on the assumption that some saccular aneurysms can be modeled as spherical elastic membranes surrounded by a viscous cerebrospinal fluid, to account for a viscohyperelastic behavior of the aneurysm. It is shown that inclusion of a "short term" viscoelastic contribution to the mechanical behavior of an aneurysm serves to increase its dynamic stability against various disturbances.

Introduction

Most intracranial saccular aneurysms remain asymptomatic for many years, perhaps decades. Nonetheless, many aneurysms rupture annually on a national basis, the unfortunate consequence of which is a high rate of mortality or devastating lasting morbidity. There is, therefore, a pressing need to understand better the natural history of

---

these lesions. Until recently, it was thought by many that saccular aneurysms enlarge and rupture due to mechanical instabilities. For example, Austin et al (1989) and Akkas (1990) suggested that these lesions suffer limit point instabilities, that is, mathematical bifurcations in their quasi-static response to distension pressures. Their findings were based on analyses of elastomeric membranes, however, not the near exponential constitutive behaviors exhibited by aneurysms. In contrast, more recent studies based on Fung and Skalak-type constitutive relations suggest that saccular aneurysms do not experience limit points (Kyriacou and Humphrey, 1996; Humphrey and Haslach, 2003).

Simkins and Stehbens (1973) and Hung and Botwin (1975) alternatively suggested that saccular aneurysms may be dynamically unstable, that they can be excited at their natural frequency by the pulsatile blood flow. Both of these studies were based on linearized elasticity despite the known nonlinear stress response exhibited by aneurysms over finite strains (Scott et al, 1972). Consequently, Shah and Humphrey (1999) studied the nonlinear elastodynamics of a sub-class of saccular aneurysms, which was defined by thin-walled spherical membranes that exhibit a Fung-type hyperelastic response over finite strains. Shah and Humphrey showed that such lesions are dynamically stable if one accounts for the effects of solid-fluid coupling, that is, the viscous cerebrospinal fluid (CSF) that often surrounds these lesions. A corollary, therefore, was that a hyperelastic lesion would not recover from small perturbations if one neglected the solid-fluid coupling or if the surrounding fluid was assumed to be inviscid (Humphrey and Haslach, 2003). A key question, therefore, is whether a surrounding viscous fluid is the only means of stabilizing such lesions.

It is well known that many soft tissues exhibit a viscoelastic response under many different conditions (Fung, 1993). Although there is no widespread agreement on a general method for modeling the viscoelasticity (e.g., Fung's quasi-linear theory of viscoelasticity describes only some of the many manifestations of the viscoelasticity; see Provenzano et al, 2000), it is widely accepted that differential (or rate) type relations are useful for describing the short-term viscoelastic response whereas integral (or heredity) type relations are useful for describing long-term creep or relaxation type responses (Pioletti and Rakotomanana, 2000). Because we are interested in the short-term response to perturbations from equilibria or during dynamic excitations, we extended our previous analysis by assuming that the lesion exhibits a nonlinear viscohyperelastic response. It is shown that the material's viscoelasticity contributes to the dynamic stability of the sub-class of lesions studied.

Methods

Following Shah and Humphrey (1999), consider an idealized class of spherical lesions surrounded by a Newtonian fluid and subjected to a periodic internal blood pressure. Let A and $a(t)$ denote the initial and deformed radii, respectively, and likewise H and $h(t)$ the initial and deformed thickness. The uniform in-plane stretch ratio is obtained as $\lambda(t) = a(t)/A$, where $\lambda \geq 1$. The 2-D deformation gradient tensor is thus given by

$$\mathbf{F} = \begin{bmatrix} \lambda(t) & 0 \\ 0 & \lambda(t) \end{bmatrix}, \tag{5.1}$$

where these stretch ratios are in the meridional and circumferential directions. The governing differential equation can be shown to be (Shah and Humphrey, 1999):

$$\left(\frac{\rho HA}{\lambda^2}+\rho_f A^2\lambda\right)\frac{d^2\lambda}{dt^2}+\frac{3}{2}\rho_f A^2\left(\frac{d\lambda}{dt}\right)^2+4\frac{\mu_f}{\lambda}\left(\frac{d\lambda}{dt}\right)+\frac{2T}{A\lambda}=P_i(t)-P_\infty(t) \quad (5.2)$$

where ρ is the density of the membrane and ρ_f and μ_f are the density and viscosity of the surrounding fluid, P_i is the internal pressure and P_∞ is the pressure of the surrounding fluid far from the lesion. T is the uniform in-plane Cauchy stress resultant that prescribes the constitutive behavior of the membrane. Haslach (2002) recently used this equation to explain the possibility of bruit formation in aneurysms.

The internal blood pressure can be specified by a Fourier series, namely (Milnor, 1989)

$$P_i(t)=P_m+\sum_{n=1}^{10}\left(A_n\cos(n\omega t)+B_n\sin(n\omega t)\right), \quad (5.3)$$

where P_m is the mean arterial blood pressure, ω is the fundamental circular frequency, and A_n and B_n are Fourier coefficients for various harmonics. Shah and Humphrey list representative values of these coefficients obtained from clinical data.

Whereas Shah and Humphrey considered a hyperelastic response for the lesion, that is, $T=T(\lambda)$ given via a Fung-type exponential strain energy function w of the form

$$w=c\left(e^Q-1\right), \qquad Q=c_1\left(E_{11}^2+E_{22}^2\right)+2c_3 E_{11}E_{22} \quad (5.4)$$

where E_{AB} are components of the 2-D Green strain tensor and c, c_1 and c_3 are material parameters (define $\Gamma\equiv c_1+c_3$), herein we consider a viscohyperelastic response:

$$\mathbf{T}=h\mathbf{t}=\frac{1}{J_{2D}}\mathbf{F}\cdot\frac{\partial w}{\partial\mathbf{E}}\cdot\mathbf{F}^T+2\mu h\mathbf{D}, \quad (5.5)$$

where $\mathbf{T}$ is the Cauchy stress resultant tensor, $\mathbf{t}$ the (3-D) Cauchy stress, $J_{2D}=\det\mathbf{F}$, μ is a "solid viscosity," and $\mathbf{D}$ is the 2-D stretching tensor. Thus, the first term on the right

hand side is the elastic contribution to the stress and the second term on the right side is the viscous contribution to the stress (Beatty and Zhou, 1991). The stretching tensor is given by $\mathbf{D} = 0.5(\mathbf{L} + \mathbf{L}^T)$, where the velocity gradient $\mathbf{L}$ is given by $\mathbf{L} \equiv \dot{\mathbf{F}} \cdot \mathbf{F}^{-1}$.

Hence, from equation (5.1), we have for the sub-class of lesions studied:

$$\mathbf{D} = \begin{bmatrix} \dfrac{1}{\lambda}\dfrac{d\lambda}{dt} & 0 \\ 0 & \dfrac{1}{\lambda}\dfrac{d\lambda}{dt} \end{bmatrix}. \tag{5.6}$$

For the Fung-elastic response (equation 5.4),

$$Q(\lambda) = \frac{1}{2}\Gamma(\lambda^2 - 1)^2 \tag{5.7}$$

and thus, invoking incompressibility to obtain $h = H/\lambda^2$, we have

$$T = c\hat{f}(\lambda) + 2\mu H \frac{1}{\lambda^3}\frac{d\lambda}{dt}, \qquad \hat{f} \equiv \Gamma e^Q(\lambda^2 - 1) \tag{5.8}$$

Shah and Humphrey non-dimensionalized equation (5.2) by choosing the following mass, length, and time scales:

$$M_s := \rho A^2 H, \qquad L_s := A, \qquad T_s := \sqrt{\frac{\rho A^2 H}{c}}. \tag{5.9}$$

Doing so here, our final differential equation becomes

$$\left(\frac{1}{x^2} + bx\right)\ddot{x} + \frac{3}{2}b\dot{x}^2 + 4m_f\frac{\dot{x}}{x} + 2\frac{\hat{f}(x)}{x} + 4md\frac{\dot{x}}{x^4} = F(\tau) \tag{5.10}$$

where the non-dimensional parameters are

$$x \equiv \lambda, \qquad \frac{dx}{d\tau} \equiv \dot{x} = \sqrt{\frac{\rho A^2 H}{c}} \left(\frac{d\lambda}{dt} \right), \qquad \frac{d^2 x}{d\tau^2} \equiv \ddot{x} = \frac{\rho A^2 H}{c} \left(\frac{d^2 \lambda}{dt^2} \right),$$

$$b \equiv \frac{\rho_f A}{\rho H}, \qquad d = \frac{H}{A}, \qquad m_f = \frac{\mu_f}{\sqrt{\rho c H}}, \qquad m = \frac{\mu}{\sqrt{\rho c H}},$$

$$F(\tau) \equiv \frac{A}{c} \left(P_i(\tau) - P_\infty \right), \qquad \text{and} \qquad \tau \equiv \frac{t}{A} \sqrt{\frac{c}{\rho H}}. \tag{5.11}$$

The governing second order differential equation (5.10) is easily solved numerically by rewriting it as a system of two first order equations:

$$\dot{y}_1 = y_2, \qquad \dot{y}_2 = \frac{F(\tau) - \dfrac{3}{2} b y_2^2 - 4 m_f \dfrac{y_2}{y_1} - 2 \dfrac{\hat{f}(y_1)}{y_1} - 4 m d \dfrac{y_2}{y_1^4}}{b y_1 + y_1^{-2}} \tag{5.12}$$

with $y_1 = x$ and $y_2 = dx/d\tau$. We used Matlab® to solve this system of differential equations. The chosen algorithm was a variable order multistep ODE solver with an adaptive step size for stiff systems (Lambert, 1991). Satisfactory results were obtained when the tolerance levels were set at 10^{-12}.

In addition to solving the full nonlinear system, it can be useful to examine the dynamic behavior about various equilibria using a linearized analysis (Humphrey, 2002). For example, if the linearized system is asymptotically stable, then the associated dynamical system is stable about that equilibrium position. Toward this end, let us expand the first order equations via a Taylor series in two variables about an arbitrary equilibrium (i.e., fixed) point $(y_1, y_2) = (\alpha, 0)$ with $F(\tau) = F_o$. That is, let

$$\dot{y}_1(y_1, y_2) = G(\alpha, 0) + \left. \frac{\partial G}{\partial y_1} \right|_{(\alpha,0)} (y_1 - \alpha) + \left. \frac{\partial G}{\partial y_2} \right|_{(\alpha,0)} (y_2 - 0) + H.O.T. \tag{5.13}$$

$$\dot{y}_2(y_1, y_2) = H(\alpha, 0) + \left.\frac{\partial H}{\partial y_1}\right|_{(\alpha,0)} (y_1 - \alpha) + \left.\frac{\partial H}{\partial y_2}\right|_{(\alpha,0)} (y_2 - 0) + H.O.T.$$

where G and H represent the functions in (5.12) and $H.O.T.$ denotes higher order terms that are neglected. Because $G(\alpha, 0) = 0$ and $H(\alpha, 0) = 0$, we get the 2 x 2 linear system:

$$\begin{bmatrix} \dot{y}_1 \\ \dot{y}_2 \end{bmatrix} = \begin{bmatrix} 0 & 1 \\ \dfrac{F_o - 2\left.\dfrac{\partial \hat{f}}{\partial y_1}\right|_{(\alpha,0)}}{\alpha^{-1} + b\alpha^2} & \dfrac{-4m_f\alpha^3 - 4md}{\alpha^2 + b\alpha^5} \end{bmatrix} \begin{bmatrix} y_1 - \alpha \\ y_2 \end{bmatrix} \tag{5.14}$$

where F_o is the constant pressure associated with the fixed point $y_1 = \alpha$, $y_2 = 0$; hence

$$F_o = 2\hat{f}(\alpha, 0)/\alpha.$$

Results

Qualitative Findings. It can be shown that, with respect to (5.14), asymptotic stability requires that tr[] < 0 and det[] > 0 (Strang, 1986). Note that the trace and determinant of this matrix for the linearized system are easily calculated as:

$$\text{tr}[] = \frac{-4m_f\alpha^3 - 4md}{\alpha^2 + b\alpha^5}, \tag{5.15}$$

and

$$\text{det}[] = \frac{\Gamma e^{Q(\alpha)}\left(4\alpha\Gamma\left(\alpha^2 - 1\right)^2 + 2\alpha + 2\alpha^{-1}\right)}{\alpha^{-1} + b\alpha^2}. \tag{5.16}$$

It is interesting to note that, given a fixed value of b, tr[] depends only on the viscous terms whereas det[] depends only on the elastic part of the constitutive relation. Because $\alpha \geq 1$, we find that det[] > 0 for all reasonable values of the material parameters (c, c_1 and c_2 are all non-negative). The tr[] < 0 provided that either m_f or m (each non-negative physically) is not zero, i.e. at least one of the viscosities, fluid or membrane, exists. If m_f
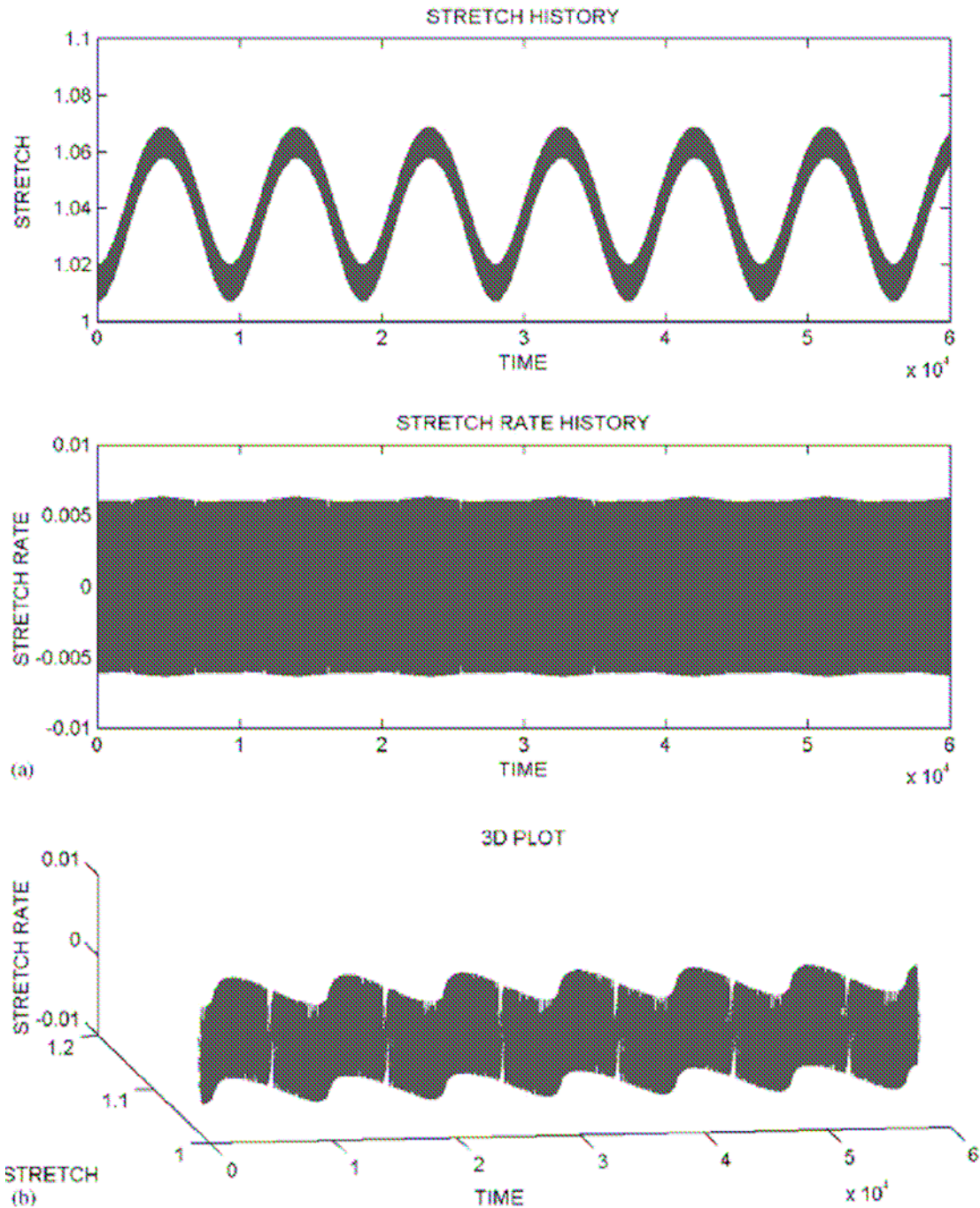
Figure 5.1. Aneurysm model without any viscosity, under sinusoidal loading. Numerical results for the full nonlinear system represent by Eq. (5.10), with a prescribed sinusoidal forcing function (Eq. 5.17) and in the absence of viscous effect ($m_f = 0, m = 0$).

Panels (a) and (b) show the predicted stretch $\lambda(\tau) = a / A$ and stretch rate $d\lambda / d\tau$. The third panel shows the phase-time plot. Note that the response is periodic but the initial disturbance persists.

and *m* are both zero, then the linearized system becomes neutrally stable and the linearization provides no information on the nonlinear system.
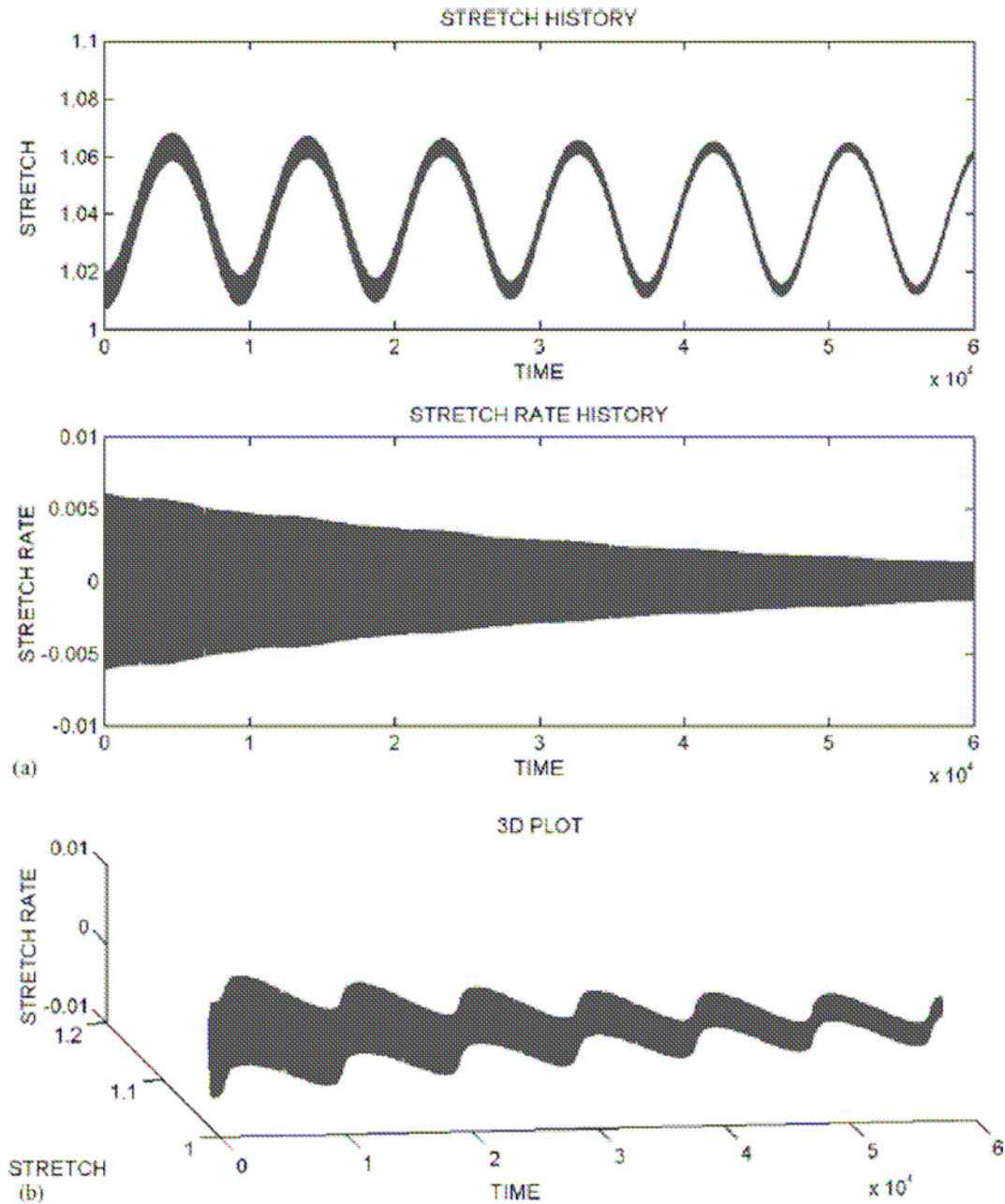

Figure 5.2. Viscoelastic aneurysm model under sinusoidal loading. Similar to Fig. 1. except that the viscous effects are included (with $m = 4m_f$). Note that the effects of the initial disturbance decay quickly, thus implying that the periodic solution is a strong attractor.

Numerical Findings. Next, consider the full nonlinear system (5.12). For the parameter values, Shah and Humphrey used: $\rho = 1050$ kg/m^3, $A = 3$ x 10^{-3} m, $H = 27.8$ x 10^{-6} m, $c = 0.88$ N/m, $\Gamma = 13$, $\rho_f = 1000$ kg/m, $\mu_f = 1.26$ x 10^{-4} Ns/m^2, and $P_\infty = 3$ mmHg. We used the same values with the exception of $c = 10.18$ N/m and $\Gamma = 23.6$ based on newer results by Seshaiyer et al (2001).

First, consider the periodic forcing function $F(\tau)$

$$F(\tau) = 2.9007\left(1 + \sin\left(\frac{4t\pi}{3\tau} - \frac{\pi}{2}\right)\right) + 1.3 \tag{5.17}$$

which was also studied by Haslach and Humphrey (2003); it simulates a sinusoidal pressurization as used in the laboratory. We consider equilibrium $(y_1, y_2) = (1.0, 0)$ but introduce an initial disturbance via the condition $(y_1, y_2) = (1.02, 0)$ at $\tau = 0$. Figure 5.1 shows the result when both m_f and m are zero. These results seem to confirm that if both the membrane and the surrounding fluid do not have a viscous response, then the stretch rate tends towards a periodic state that includes the disturbance. That is, the response is not asymptotically stable. Although not shown, the case for $m_f \neq 0$ and $m = 0$ recovers qualitatively that found previously by Shah and Humphrey (1999), but the effect of the disturbance disappears sooner given the values of c and Γ reported by Seshaiyer et al (2001).

We then considered non-zero values of m by letting it equal some constant multiple of m_f. Figure 5.2 shows the result when $m = 4m_f$. Simply put, as m is increased, the effects of the disturbance decay more rapidly. Regardless of the rate of decay, the inclusion of wall viscoelasticity augments the stabilizing effect of a viscous CSF.
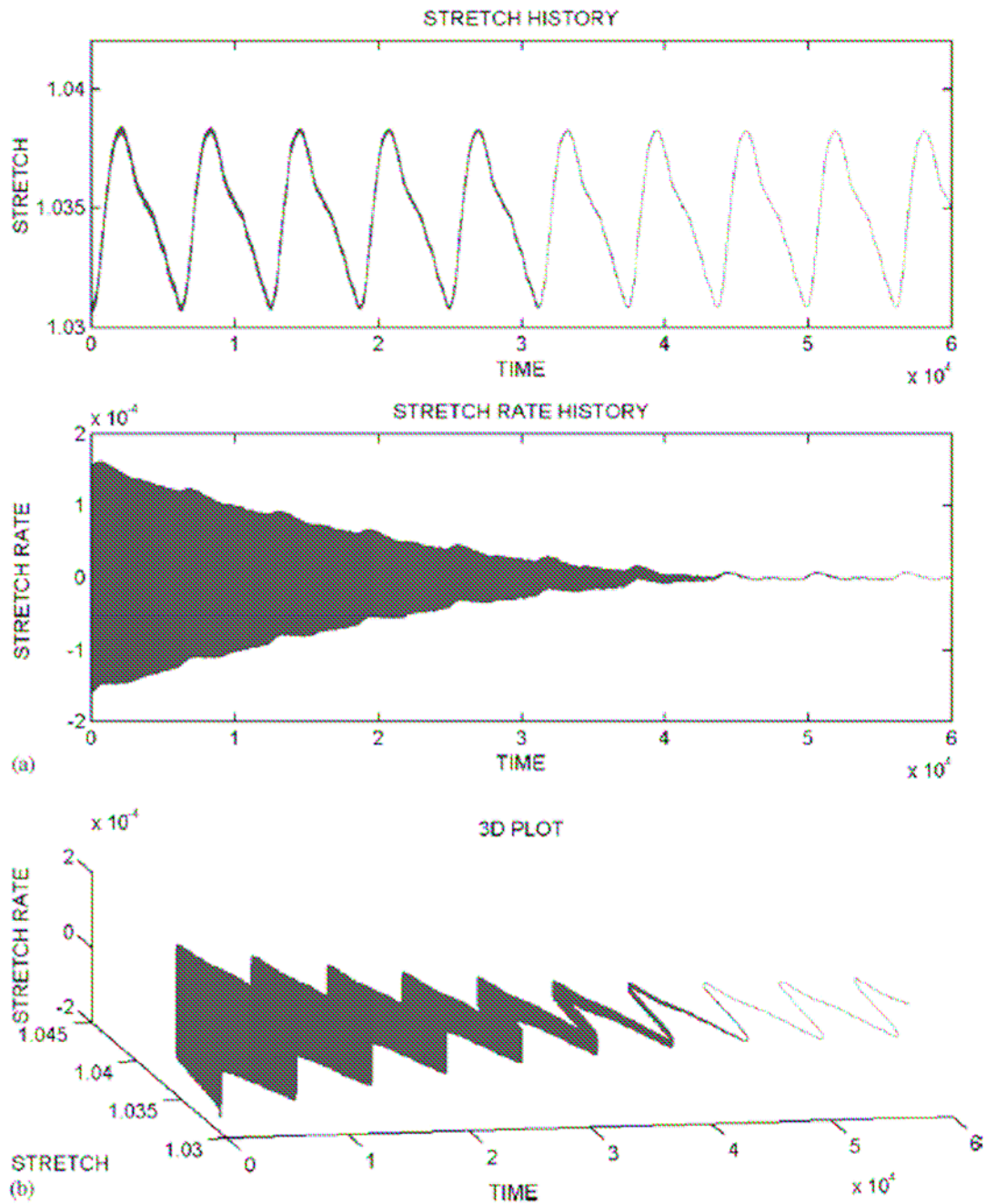
Figure 5.3. Viscoelastic aneurysm model under physiological pressure. Similar to Fig. 2, except for a physiological forcing function (Eq. 5.3). The effects of the initial disturbance again decay in the presence of viscous effects.

Second, consider $F(\tau)$ consistent with equation (5.3) with $P_m = 90.0$, $A_1 = -7.1262564$, $A_2 = -3.0808384$, $A_3 = -0.12975114$, $A_4 = -0.20527592$, $A_5 = 0.066159552$, $A_6 = 0.0020829707$, $A_7 = 0.032060151$, $A_8 = -0.056227174$,

A_9 = -0.014961972, A_{10} = -0.041793236, B_1 = 4.6403985, B_2 = -1.180785,

B_3 = -0.56407837, B_4 = -0.34629119, B_5 = -0.12007571, B_6 = -0.041573029,

B_7 = -0.10536408, B_8 = -0.048787851, B_9 = 0.077850393, and B_{10} = 0.040598301, all in

mmHg, and non-dimensionalized via (5.11). The initial disturbance is given by (y_1, y_2) =

(1.032, 0) at $\tau = 0$. The results when $m = 4m_f$ are shown in Figure 5.3, wherein we again

see that the effects of the disturbance disappear quickly.

Exact Findings. In addition to the aforementioned qualitative findings, the

linearized system of two ordinary differential equations can also be solved as follows: let

ζ_1 and ζ_2 be the two eigenvalues of the matrix in (5.14). Clearly, these eigenvalues are

complex-valued if $4\det[] > (\text{tr}[])^2$, i.e. if:

$$\Gamma e^{Q(\alpha)} \alpha^3 \left(1 + b\alpha^3\right)\left(\Gamma\alpha^3(\alpha^2 - 1)^2 + \tfrac{1}{2}\alpha + \tfrac{1}{2}\alpha^{-1}\right) > \left(m_f\alpha^3 + md\right)^2. \tag{5.18}$$

Equation (5.18) holds for all physically realistic values of the non-dimensional viscosities

m_f and m, hence the eigenvalues are complex-valued. Because

$$\det[] = \zeta_1\zeta_2, \quad \text{tr}[] = \zeta_1 + \zeta_2. \tag{5.19}$$

and det[] and tr[] are real-valued, these eigenvalues must be complex conjugates. We

write (with $p, q \geq 0$):

$$\zeta_1 = -p + qi, \quad \zeta_2 = -p - qi. \tag{5.20}$$

The general solution of the linearized system (5.14) is thus

$$y_1 = e^{-p\tau}\left((\kappa_1 + \kappa_2)\cos(q\tau) + i(\kappa_1 - \kappa_2)\sin(q\tau)\right), \quad y_2 = \frac{dy_1}{d\tau}. \tag{5.21}$$

Our solution must be real-valued as well, hence the constants $\kappa_1 = \kappa_2 = \kappa$ and we obtain

the solution

$$y_1 = 2\kappa e^{-p\tau}\cos(q\tau), \quad y_2 = -2\kappa e^{-p\tau}\left(p\cos(q\tau) + q\sin(q\tau)\right). \tag{5.22}$$

This solution is the limiting case for the dynamical system (5.12). For instance, if we solve (5.12) numerically with an initial condition $y_1 = \alpha + \delta_1$, $y_2 = \delta_2$, where the δ's are small perturbations from an equilibrium state, then the solution of (5.12) will tend towards (5.22). In the special case where $m_f = m = 0$, we get the periodic solution set about the fixed point:

$$y_1 = 2\kappa \cos(q\tau), \qquad y_2 = -2\kappa q \sin(q\tau), \tag{5.23}$$

consistent with the numerical findings. In other words, the dynamical system is (asymptotically) stable only if one or both of the viscosities is non-zero (i.e. $p \neq 0$).

Discussion

Intracranial saccular aneurysms exist in a myriad of sizes and shapes, and they likely exhibit complex anisotropic and inhomogeneous material behaviors (Humphrey and Canham, 2000). Clearly, therefore, we have examined only one special sub-class of lesions, those having a nearly spherical geometry and homogenous, isotropic properties. Although the latter is likely a gross approximation (Ryan and Humphrey, 1999), it allowed us to study the first order elastodynamics of a sub-class of saccular aneurysms. Indeed, as discussed by Shah and Humphrey (1999), finite element results support the utility of studying this sub-class of spherical lesions.

As noted earlier, the pulsatility of the blood pressure has been implicated for nearly 30 years as a possible cause of aneurysmal enlargement or rupture. Such suggestions were based on casual observations or purely linear analyses, however, and thus needed a more rigorous study. Towards this end, Shah and Humphrey (1999) were the first to consider the effects of the nonlinear elastic behavior that aneurysms are known to exhibit over finite strains as well as the possible effects of solid-fluid coupling due to a

surrounding viscous CSF. The governing differential equation for a spherical lesion was solved numerically and the results were interpreted using the geometric approach of Poincare'. It was found that such lesions are dynamically stable; it was also suggested that including the viscoelastic properties of the wall might further stabilize the lesion. The latter has now been verified by the present results.

Although a numerical method is necessary to solve a complex nonlinear differential equation such as (5.10), and parametric studies can provide insight into the effects of different contributors to the physics, it is generally prudent to supplement numerical results with analytical ones when possible. For example, if one linearizes a dynamical system about a fixed point, then the nonlinear system is stable about that fixed (equilibrium) point if the associated linearized system is asymptotically stable. We further extended the results of Shah and Humphrey by considering such a linearization. These findings are particularly important for they reveal *how* the constitutive equation for the nonlinearly elastic behavior of the wall (equation 5.16) and the separate viscous effects (equation 5.15) individually affect the dynamic stability for *all* fixed points α. In particular, equation (5.15) reveals that the dynamical system can only be stable if either the CSF is viscous or the aneurysm is viscoelastic (i.e., either m or m_f has to be non-zero for tr[] < 0). It is remarkable that any non-zero value, however small, of either viscosity can stabilize the system – larger values simply allow the periodic solution to be regained sooner following a disturbance, which is supported by the numerics (Figure 2). Conversely, the absence of viscous dissipation renders the linearized system neutrally stable (equation 5.15), which does not provide reliable information on the nonlinear system. Equation (5.23) supports the numerics (Figure 1), however, which suggest an

unstable response in the absence of any viscosity. This is certainly intuitive. Finally, equation (5.16) reveals that all Fung-elastic spheres can be stable, again with the larger values of the material parameters simply modifying the response quantitatively, not qualitatively. These analytical findings are especially important for they engender confidence in the present numerical findings as well as those in Shah and Humphrey (1999). As it is well known, one must interpret numerical findings cautiously, particularly when they are highly sensitive to the assumed tolerance levels (e.g., numerical damping) and the type of solver (e.g., we used an adaptive step-size Runge-Kutta algorithm for stiff systems). Collectively, the present methods – numerical solution of the fully nonlinear system, qualitative interpretation of the linearized system, and exact solution of the linearized system – strongly suggest that the nonlinearly elastic behavior of the lesion, the presence of intrinsic wall viscoelasticity, and the presence of a viscous CSF all serve to stabilize saccular aneurysms under the dynamical loads imposed during a cardiac cycle. Such stability is consistent, of course, with reports that only a small percentage of lesions actually rupture (Humphrey and Canham, 2000).

In conclusion, we submit that although the elastodynamics of aneurysms could be studied for more complex geometries and material properties, it appears that attention should be directed towards studies of the kinetics of growth and remodeling. Research on growth and remodeling has become a topic of increased attention (e.g. see Taber, 1995; Humphrey and Rajagopal, 2002), but much remains to be accomplished both with regard to the fundamental constitutive framework and the solution of specific initial-boundary value problems.

CHAPTER VI

SUMMARY AND RECOMMENDATIONS

Vision is arguably the most important and most used among the human senses, thus preventing loss of vision is a paramount concern among all individuals. It comes as no surprise that a significant portion of the health care budget concerns ophthalmology. Cataract surgery, for instance, is the number one procedure in the United States with over a million operations each year. Consequently, eye research plays a huge role in the improvement of surgical techniques and development of vision technology.

One particular topic in ophthalmology that has received moderate attention but limited results is the biomechanics of the lens capsule, the membrane that envelopes the lens and presents most of the problems associated with cataract surgery. Prior studies in lens capsule mechanics are largely based on 1-dimensional stress-strain tests, and assume linear elasticity, homogeneity, and isotropy. This obvious simplification provides an adequate preliminary study on the subject, but that is all they are, and later investigators should be reminded not to accept these assumptions.

In this dissertation, the lens capsule is modeled using less restrictive assumptions, i.e. the material is non-homogenous, anisotropic and nonlinearly hyperelastic, using data based on 2-dimensional pressure-strain tests in the in situ configuration. The results of our finite element computations show that our nonlinear elastic model captures the behavior of the lens capsule reasonably well, which exhibits regionally varying anisotropy. We show that this anisotropy and non-homogeneity of the lens capsule is critical in preserving its geometry and maintaining a lower and more uniform stress field.

We further demonstrate numerically the effects of a capsulorhexis on altering the geometry and stress field of the lens capsule.

The results presented in this study for the first time bring our understanding of the mechanics of the lens capsule to a higher level. Nevertheless, we have only started to appreciate the underlying mechanics of the lens capsule and how it affects cataract surgery. More work is needed, particularly in identifying how various alterations in the lens capsule geometry may lead to a more favorable stress profile. We have not considered the boundary effects of devices such as intraocular lens (IOL) haptics or capsular bend rings on the behavior of the lens capsule after post surgery. Future work may also consider modeling lens capsule accommodation and artificially replicating this phenomenon with an IOL. Finally, additional models (beyond Fung and Choi-Vito) need to be developed.

REFERENCES

Akkas, N., 1990. Aneurysms as a biomechanical instability problem. In: Mosora, F. (Ed.), Biomechanical Transport Processes. Plenum Press, New York, pp 303-311.

Apple, D.J., Peng, Q., Visessook, N., Werner, L., Pandey, S.K., Escobar-Gomez, M., Ram, J., Auffarth, G.U., 2001. Eradication of posterior capsule opacification: documentation of a marked decrease in Nd:YAG laser posterior capsulotomy rates noted in an analysis of 5416 pseudophakic human eyes obtained postmortem. Ophthalmology 108, 505-518.

Austin, G.M., Schievink, W., Williams, R., 1989. Controlled pressure-volume factors in the enlargement of intracranial saccular aneurysms. Neurosurgery 24, 722-730.

Beatty, M.F., Zhou, Z., 1991. Universal motions for a class of viscoelastic materials of differential type. Continuum Mechanics and Thermodynamics 3, 169-191.

Brown, N., 1973. The change in shape and internal form of the lens of the eye on accommodation. Experimental Eye Research 15, 441-459.

Burd, H.J., Judge, S.J., Flavell, M.J., 1999. Mechanics of accommodation of the human eye. Vision Research 39, 1591-1595.

Burd, H.J., Judge, S.J., Cross, J.A., 2002. Numerical modeling of the accommodating lens. Vision Research 42, 2235-2251.

Choi, H.S., Vito, R.P., 1990. Two-dimensional stress-strain relationship for canine pericardium. Journal of Biomechanical Engineering 112, 153-159.

Cowin, S.C., 2000. How is tissue built? Journal of Biomechanical Engineering 122, 553-569.

David, G., Humphrey, J.D., 2003. Further evidence for the dynamic stability of intracranial saccular aneurysms. Journal of Biomechanics 36, 1143-1150.

David, G., Humphrey, J.D., 2004. Redistribution of stress due to a circular hole in a nonlinear anisotropic membrane. Journal of Biomechanics 37, 1197-1203.

Foster, A., 1999. Cataract—a global perspective: output, outcome and outlay. Eye 13, 449-453.

Fung, Y.C., 1990. Biomechanics: Motion, Flow, Stress and Growth. Springer-Verlag, New York.

Fung, Y.C., 1993. Biomechanics: Mechanical Properties of Living Tissues. Springer-Verlag, New York.

Gruttman, F., Taylor, R.L., 1992. Theory and finite element formulation of rubberlike membrane shells using principal stretches. International Journal for Numerical Methods in Engineering 35, 1111-1126.

Haslach, H.W., 2002. A nonlinear dynamical mechanism for bruit generation by an intracranial saccular aneurysm. Journal of Mathematical Biology 45, 441-460.

Haslach, H.W., Humphrey, J.D., 2003. The dynamics of biological soft tissue or rubber, internally pressurized spherical membranes surrounded by a fluid. International Journal of Non-linear Mechanics 39, 399-420.

Heistand, M.R., Pedrigi, R.M., Delange, S.L., Dziezyc, J., Humphrey J.D., 2005a. Multiaxial mechanical behavior of the porcine anterior lens capsule. Biomechanics and Modeling in Mechanobiology (accepted).

Heistand, M.R., Pedrigi, R.M., Dziezyc, J., Humphrey, J.D., 2005b. Redistribution of strain and curvature in the porcine anterior lens capsule following a continuous circular capsulorhexis. Journal of Biomechanics (accepted).

Holzapfel, G.A., 2000. Nonlinear Solid Mechanics: A Continuum Approach for Engineering. Wiley & Sons, Chichester, England.

Humphrey, J.D., Canham, P.B., 2000. Structure, mechanical properties, and mechanics of intracranial saccular aneurysms. Journal of Elasticity 61, 49-81.

Humphrey, J.D., 2002. Cardiovascular Solid Mechanics: Cells, Tissues, and Organs, Springer-Verlag, New York.

Humphrey, J.D., Rajagopal, K.R., 2002. A constrained mixture model for growth and remodeling of soft tissues. Mathematical Modeling and Methods in Applied Science 12, 407-430.

Humphrey, J.D., 2003. Native properties of cardiovascular tissues: guidelines for functional tissue engineering. In: F. Guilak, D.L. Butler, S.A. Goldstein, D.J. Mooney (Eds.), Functional Tissue Engineering, Springer, New York.

Humphrey, J.D., Haslach, H.W., 2003. Elastodynamics of saccular aneurysms: Solid-fluid interactions and constitutive relations. In: M. W. Collins (Ed.), Wall/Fluid Interactions in Physiologic Flows. WIT Press, Southampton.

Hung, E.J.N., Botwin, M.R., 1975. Mechanics of rupture of cerebral saccular aneurysms. Journal of Biomechanics 8, 385-392.

Krag S., Thim, K., Corydon, L., Kyster, B., 1994. Biomechanical aspects of the anterior capsulotomy. Journal of Cataract and Refractive Surgery 20, 410-416.

Krag S., Andreassen, T.T., 1996. Biomechanical measurements of the porcine lens capsule. Experimental Eye Research 62, 253-260.

Krag S., Olsen, T., Andreassen, T.T., 1997. Biomechanical characteristics of the human anterior lens capsule in relation to age. Investigative Ophthalmology and Visual Science 38, 357-363.

Krag, S., 1999. Biomechanical measurements of the lens capsule. Acta Ophthalmologica Scandinavica 77, 364.

Krag S., Andreassen, T.T., 2003. Mechanical properties of the human lens capsule. Progress in Retinal and Eye Research 22, 749-767.

Kyriacou, S.K., Humphrey, J.D., 1996. Influence of size, shape and properties on the mechanics of axisymmetric saccular aneurysms. Journal of Biomechanics 29, 1015-1022. Erratum, 30 (1997) 761.

Kyriacou, S.K., Schwab, C., Humphrey, J.D., 1996. Finite element analysis of nonlinear orthotropic hyperelastic membranes. Computational Mechanics 18, 269-278.

Lambert, J.D., 1991. Numerical Methods for Ordinary Differential Systems. Wiley, New York, pp. 149-231.

Milnor, W.R., 1984. Hemodynamics, 2nd Edition, Williams & Wilkens, Baltimore.

Oden, J.T., 1972. Finite Elements of Nonlinear Continua. McGraw-Hill, New York.

Pioletti, D.P., Rakotomanana, L.R., 2000. Non-linear viscoelastic laws for soft biological tissues. European Journal of Mechanics (A/Solids) 19, 749-759.

Provenzano, P.P., Lakes, R.S., Corr, D.T., Vanderby, R., 2002. Application of nonlinear viscoelastic models to describe ligament behavior. Biomechanical and Modeling Mechanobiology 1, 45-57.

Rivlin, R.S., Thomas, A.G., 1951. Large elastic deformations of isotropic materials VIII. Strain distribution around a hole in a sheet. Philosophical Transactions of the Royal Society (London) A. 243, 289-298.

Ryan J.M., Humphrey, J.D., 1999. Finite element based predictions of preferred material symmetries in saccular aneurysms. Annals of Biomedical Engineering 27, 641-647.

Sacks, M.S, 1999. A method for planar biaxial mechanical testing that includes in-plane shear. Journal of Biomechanical Engineering 121, 551-555.

Sacks, M.S., Sun, W., 2003. Multiaxial mechanical behavior of biological materials. Annual Reviews of Biomedical Engineering 5, 251-284.

Scott, S., Ferguson, G.G., Roach, M.R., 1972. Comparison of the elastic properties of human intracranial arteries and aneurysms. Canadian Journal of Physiology and Pharmacology 50, 328-332.

Shah A.D., Humphrey, J.D., 1999. Finite strain elastodynamics of saccular aneurysms. Journal of Biomechanics 32, 593-599.

Seshaiyer P., Hsu, F.P.K., Shah, A.D., Kyriacou, S.K., Humphrey, J.D., 2001. Multiaxial mechanical behavior of human saccular aneurysms. Computer Methods in Biomechanics and Biomedical Engineering 4, 281-290.

Seshaiyer, P., Humphrey, J.D., 2003. A sub-domain inverse finite element characterization of hyperelastic membranes including soft tissues. Journal of Biomechanics 125, 363-371.

Simkins, T.E., Stehbens, W.E., 1973. Vibrational behavior of arterial aneurysms. Letters in Applied Engineering Science 1, 85-100.

Strang, G., 1986. Introduction to Applied Mathematics. Cambridge University Press, Cambridge.

Szabo, B.A., Babuska, I., 1991. The Finite Element Method. Wiley & Sons, New York.

Taber, L.A., 1995. Biomechanics of growth, modeling and morphogenesis. Applied Mechanics Reviews 48, 487-545.

Tranquillo, R.T., Murray, J.D., 1992. Continuum model of fibroblast-driven wound contraction: inflammation-mediation. Journal of Theoretical Biology 158, 135-172.

Varley, E., Cumberbatch, E., 1980. Finite deformations of elastic materials surrounding cylindrical holes. Journal of Elasticity 10, 341-405.

Verma, P.D.S., Rana, O.H., 1978. Radial deformation of a plane sheet containing a circular hole or inclusion. International Journal of Nonlinear Mechanics 13, 199-260.

APPENDIX

It would seem that a sufficient condition for convexity of the strain-energy function (2.3) is that $c_1, c_2, c_3 > 0$ whenever $c > 0$. This is not, however, sufficient to ensure proper behavior of the model. To illustrate, consider the uniaxial strain test in the 1-direction shown previously. From (2.25) we have

$$
\begin{aligned}
T_{11} &= \frac{1}{\det \mathbf{F}} F_{11}^2 \frac{\partial w}{\partial E_{11}} \\
&= c \frac{\lambda}{\mu} \left(2c_1 E_{11} e^{c_1 E_{11}^2} + 2c_3 E_{22} e^{c_3 E_{11} E_{22}} \right)
\end{aligned}
\tag{A1}
$$

We assume small strains. Let $E_{11} = \delta$. We can then estimate $E_{22} = -\delta$. Note that the enclosed quantity becomes:

$$
2\delta \left(c_1 \exp\left(c_1 \delta^2 \right) - c_3 \exp\left(-c_3 \delta^2 \right) \right).
\tag{A2}
$$

For small strains, the exponential becomes close to 1. This means that if $c_3 > c_1$ then the Cauchy stress in the direction of the stretch becomes negative. Using a similar argument for the other direction, we obtain a weak condition for the material parameters as:

$$
c_1 > c_3 \text{ and } c_2 > c_3.
\tag{A3}
$$

This restriction is weak in the sense that it guarantees that the material behaves properly, but a less restrictive condition may be available.

For the Fung pseudostrain-energy function given by (2.2), uniaxial strain in the 1-direction as in (2.22) gives

$$
\begin{aligned}
T_{11} &= \frac{1}{\det \mathbf{F}} F_{11}^2 \frac{\partial w}{\partial E_{11}} \\
&= 2c \frac{\lambda}{\mu} e^Q \left(c_1 E_{11} + c_3 E_{22} \right)
\end{aligned}
\tag{A4}
$$

Using a similar estimate of $E_{11} = \delta$ and $E_{22} = -\delta$, we have

$$T_{11} = 2c\frac{\lambda}{\mu}e^{Q}\delta(c_1 - c_3) \tag{A5}$$

Since all the other quantities are nonnegative, then we must have $c_1 > c_3$. A similar argument shows $c_2 > c_3$ as a weak condition for the Fung model. Note that the parameter restriction $c_1, c_2 > c_3$ automatically satisfies the convexity restriction (Holzapfel) given by $c_1 c_2 > c_3^2$.

VITA

Name: Fredegusto Guido David

Address: c/o Biomedical Engineering Department, Texas A&M University, College Station, TX 77840

Email: vantugo@hotmail.com

Education: B.S. Mathematics, University of the Philippines, 1991
M.S. Applied Mathematics, University of the Philippines, 1993
M.S. Mathematics, Texas A&M University, 2000
Ph.D. Biomedical Engineering, Texas A&M University, 2005